



Available online at www.sciencedirect.com

ScienceDirect

Geochimica et Cosmochimica Acta 203 (2017) 216-234

Geochimica et Cosmochimica Acta

www.elsevier.com/locate/gca

An introduction of Markov chain Monte Carlo method to geochemical inverse problems: Reading melting parameters from REE abundances in abyssal peridotites

Boda Liu, Yan Liang*

Department of Earth, Environmental and Planetary Sciences, Brown University, Providence, RI 02912, United States

Received 16 June 2016; accepted in revised form 31 December 2016; Available online 11 January 2017

Abstract

Markov chain Monte Carlo (MCMC) simulation is a powerful statistical method in solving inverse problems that arise from a wide range of applications. In Earth sciences applications of MCMC simulations are primarily in the field of geophysics. The purpose of this study is to introduce MCMC methods to geochemical inverse problems related to trace element fractionation during mantle melting. MCMC methods have several advantages over least squares methods in deciphering melting processes from trace element abundances in basalts and mantle rocks. Here we use an MCMC method to invert for extent of melting, fraction of melt present during melting, and extent of chemical disequilibrium between the melt and residual solid from REE abundances in clinopyroxene in abyssal peridotites from Mid-Atlantic Ridge, Central Indian Ridge, Southwest Indian Ridge, Lena Trough, and American-Antarctic Ridge. We consider two melting models: one with exact analytical solution and the other without. We solve the latter numerically in a chain of melting models according to the Metropolis-Hastings algorithm. The probability distribution of inverted melting parameters depends on assumptions of the physical model, knowledge of mantle source composition, and constraints from the REE data. Results from MCMC inversion are consistent with and provide more reliable uncertainty estimates than results based on nonlinear least squares inversion. We show that chemical disequilibrium is likely to play an important role in fractionating LREE in residual peridotites during partial melting beneath mid-ocean ridge spreading centers. MCMC simulation is well suited for more complicated but physically more realistic melting problems that do not have analytical solutions. © 2017 Elsevier Ltd. All rights reserved.

Keywords: Markov chain Monte Carlo; Disequilibrium; Fractional melting; Dynamic melting; Abyssal peridotite; Rare earth element; Diffusion; Clinopyroxene; Geochemical inverse problem

1. INTRODUCTION

The abundance and distribution of trace elements in primitive basalts and residual peridotites are important to understanding mantle source compositions and mantle melting processes. During partial melting, abundances of trace elements in interstitial melt and residual solid are redistributed or fractionated in accordance with their solid-melt partition coefficients, extent of melting, and style of melt extraction. Interpretations of trace element data, therefore, depend critically on melting models, melting parameters, and mantle source composition. Simple melting models that have frequently been used in the interpretation of trace element data in basalts and residual peridotites include batch melting, incremental batch melting, fractional melting, and dynamic melting models (e.g., Albarède, 1995; Shaw, 2006; Zou, 2007). A common feature of these simple melting models is that they all have explicit analytical solu-

E-mail address: Yan Liang@brown.edu (Y. Liang).

^{*} Corresponding author.

tions relating melt and residual solid compositions to the degree of melting experienced by the solid. In more complicated but physically more realistic melting models, such as double porosity melting models and disequilibrium melting models (Qin, 1992; Iwamori, 1993a,b, 1994; Lundstrom, 2000; Ozawa, 2001; Jull et al., 2002; Van Orman et al., 2002; Liang and Parmentier, 2010; Liang and Peng, 2010), there are no analytical solutions to the mass conservation equations governing the fractionation of a trace element in the partial melt and residual solid, except a few special cases. Numerical methods are used to solve the governing equations (Richter, 1986; Jull et al., 2002; Spiegelman and Kelemen, 2003).

Interpretations of basalt and peridotite trace element data typically follow one of two approaches or methods (Allegre and Minster, 1978): forward method and inverse method. In the forward approach, one calculates trace element abundances in the melt and residual solid or mineral (often clinopyroxene) for a range of melting parameters (e.g., 0-20% melting, 0-2% trapped melt in the dynamic melting model) using several melting models for a group of trace elements in question (e.g., REE and HFSE). Results from the forward calculation are then compared with measured trace element data on a spider diagram, element vs. element diagrams (e.g., Ti vs. Zr), element vs. element ratio diagrams (e.g., Sm/Yb vs. Yb), or element ratio vs. element ratio diagrams (e.g., Ti/Zr vs. Sm/Yb). The model is deemed acceptable or successful if part or all of the observed trace element data in samples included in the study can be explained or bracketed by those predicted by the forward model calculations. If the melting model fails to explain part of the observed data (e.g., LREE enrichment in residual clinopyroxene), additional processes such as late-stage melt impregnation or mantle metasomatism are invoked and further tested. Such forward modeling followed by direct comparison with measured data has been widely used in the interpretation of trace element data from primitive basalts and residual peridotites (e.g., Langmuir et al., 1977, 2006; McKenzie, 1985; Johnson et al., 1990; Kelemen et al., 1997; Niu and Hékinian, 1997; Shimizu, 1998; Lundstrom, 2000; Hellebrand et al., 2002; Jull et al., 2002; Van Orman et al., 2002; Spiegelman and Kelemen, 2003; Niu, 2004; Kelley et al., 2006; Liang and Parmentier, 2010; Brunelli et al., 2006, 2014).

In the inverse approach, the melting parameters are extracted from measured trace element data through least squares analysis (Allegre and Minster, 1978; Minster and Allegre, 1978; Hofmann and Feigenson, 1983; McKenzie and O'Nions, 1991; Albarède, 1995; Zou, 2007). Here one minimizes a Chi-square defined by the measured trace element concentrations and those predicted by the melting model and weighted by data quality. Early applications of the inverse method to mantle melting follow the strategies outlined in Minster and Allegre (1978) and Hofmann and Feigenson (1983). Given the relatively poor knowledge of mineral-melt partition coefficients, melting reaction, and mantle composition and mineralogy at the time, these early studies used the batch melting model and incompatible trace element ratios and abundances in basalts to invert for bulk solid-melt partition coefficients and mantle mineralogy (Feigenson et al., 1983; Hofmann and Feigenson, 1983; Ormerod et al., 1991; Feigenson and Carr, 1993). McKenzie and coworkers (McKenzie and O'Nions, 1991, 1995, 1998; Watson and McKenzie, 1991; White et al., 1992; Watson, 1993; Tainton and McKenzie, 1994; McKenzie et al., 2004) applied Backus and Gilbert (1968)'s optimization technique (for a summary see Parker, 1977) to invert melt fraction and distribution in a melting column from REE abundances in basalts. In a more restricted case in which the melting model has explicit analytical expression, the nonlinear least squares method (also called the linearized least squares method, abbreviated as "LS" hereafter, Tarantola, 2005) is very useful in inverting all model parameters simultaneously. There are only a few mantle melting studies that took the nonlinear least squares approach. Liang and Peng (2010) used the nonlinear least squares method and a steady-state double porosity model to invert the degree of melting and the extent of melt extraction from REE and Y abundances in residual clinopyroxene from the Central Indian Ridge (data reported by Hellebrand et al., 2002). LREE abundances in half of the sample set are too high to be consistent with the steady-state model. Liang and Liu (2016) further examined this problem using a disequilibrium perfect fractional melting model. They showed that a small extent of chemical disequilibrium, due to slow diffusion of LREE in clinopyroxene, can explain the elevated LREE abundances in residual clinopyroxenes in the abyssal peridotites. They also noted a positive correlation between the degree of melting and the extent of chemical disequilibrium and attributed it to an increase in melting rate and a decrease in REE diffusion rate along the melting path. However, given the nonlinear nature of the melting problem and the simplified melting model used, it is not clear if this is a robust observation for decompressional melting along a melting column when additional melting parameters are considered. For example, in a more general case of dynamic melting, a small fraction of melt is retained in the melting column, which may affect the interpretation of other melting parameters through nonlinear trade-offs among the melting parameters. Although it is straightforward to develop a disequilibrium dynamic melting model by relaxing model assumptions, the governing mass conservation equations are nonlinear and do not have explicit analytical solutions (e.g., Liang, 2003), which limits application of the nonlinear least squares inversion method. If more complicated melting models are used to interpret trace element data, robust inversion methods are needed.

The purpose of this study is twofold: (1) to introduce Markov chain Monte Carlo (MCMC) methods to geochemical inverse problems related to trace element fractionation during mantle melting, and (2) to further test the robustness of the positive correlation between the degree of melting and the extent of chemical disequilibrium noted earlier. Conservation equations for trace element fractionation during concurrent melting, melt migration and meltrock interaction generally do not have analytical solutions and hence cannot be easily solved using least squares inversion methods. MCMC methods are a class of powerful statistical tools for solving inverse problems that arise from a

wide range of applications, such as physics, chemistry, computational biology, computer science, financial engineering, among others (Robert and Casella, 2004; Liu, 2008). In Earth sciences, applications of MCMC methods are primarily in the field of geophysics (Sambridge and Mosegaard, 2002). MCMC methods have several advantages over the least squares methods in inverting melting parameters from trace element abundances in basalts and mantle rocks. First, MCMC methods can handle any model or equation that has no explicit analytical solution. Second, MCMC methods can take advantage of prior knowledge of the system in question (e.g., based on previous studies, we know mantle melting is near fractional) and further improve the estimation of model parameters based on new observations in hand, an important feature that nonlinear least squares inversion methods do not have. Third, MCMC algorithms can handle multiple local minima in nonlinear inverse problems that may pose a challenge to nonlinear least squares analysis. Finally, MCMC simulations can provide insights into uncertainties of model parameters with nonlinear trade-off.

The remaining part of this paper is organized as follows. In Section 2, we outline the procedure of a widely used MCMC method that is based on the Metropolis-Hastings algorithm. In Section 3, we use two melting models and abyssal peridotite data from Central Indian Ridge to highlight the advantages of the MCMC method: a disequilibrium fractional melting model that has an explicit analytical solution, and a more general model of disequilibrium dynamic melting that has no analytical solution. In Sections 4 and 5, we use the MCMC method and the disequilibrium dynamic melting model to invert melting parameters from REE and Y abundances in clinopyroxene in abyssal peridotites from four additional ridge systems: Mid-Atlantic Ridge, Southwest Indian Ridge, Lena Trough, and American-Antarctic Ridge. We show that a robust positive correlation between the degree of melting and the extent of disequilibrium for REE in clinopyroxene exists in abyssal peridotites from Southwest Indian Ridge and Central Indian Ridge and discuss our results in the context of adiabatic mantle melting. Finally in Section 6, we outline potential applications of MCMC methods to more general cases of mantle melting.

2. MARKOV CHAIN MONTE CARLO METHOD

Markov chain Monte Carlo method was first introduced by Metropolis et al. (1953) to study macroscopic equilibrium of interacting molecules in statistical mechanics. The Metropolis algorithm was extended by Hastings (1970) for more general cases. The MCMC method uses the posterior distribution to estimate the probability of model parameters given data as constraints. Here posterior distribution is the distribution of unknown model parameters based on the observed data. By randomly generating trial models and accepting or rejecting the trial model in accordance with a transition probability, the Metropolis–Hastings algorithm produces a chain of models whose distribution converges to posterior distribution, i.e., the desired parameters that reproduce the observed data.

2.1. The estimate of model parameters: posterior distribution

To estimate a model parameter is to determine the probability distribution of the model parameter (i.e., their bestestimated values and associate uncertainties) given data as constraints. For example, REE abundances in an abyssal peridotite may suggest that 10% melting is more likely to explain the observed REE data than 5% melting. In other words, the degree of melting (F) has a higher probability at 10% than at 5%. There exists a posterior distribution that specifies the probability of F within a range of values. There are two ways to describe posterior distribution: (1) a probability density function characterized by a finite number of parameters, and (2) a sample set consisting of a large number of model parameters belonging to the posterior distribution. The nonlinear least squares method utilizes the former with a normal distribution (characterized by two parameters: the mean and the standard deviation), whereas MCMC methods resort to the latter which is more general. The mean and standard deviation of the sample of model parameters acquired by MCMC methods are consistent with the nonlinear least squares method if the posterior distribution is a normal distribution.

Let \mathbf{m} be a vector of model parameters. For the case of disequilibrium fractional melting model used in Section 3.2, $\mathbf{m} = (F, \varepsilon)$, where ε is a measure of chemical disequilibrium defined in the next section. Let \mathbf{C} be the data or concentration vector with each component C_i as the concentration of element i. In Bayesian statistics, the posterior probability of a model, $p(\mathbf{m}|\mathbf{C})$, is proportional to the product of the data-independent prior probability of this model, $\theta(\mathbf{m})$, and the likelihood of the model in observing the data, $\mathbf{L}(\mathbf{C}|\mathbf{m})$ (Grandis et al., 1999; Sambridge and Mosegaard, 2002; Robert and Casella, 2004; Tarantola, 2005; Korenaga and Karato, 2008), viz.,

$$p(\mathbf{m}|\mathbf{C}) = A \cdot L(\mathbf{C}|\mathbf{m}) \cdot \theta(\mathbf{m}), \tag{1}$$

$$\int_{\mathbf{m}} p(\mathbf{m}|\mathbf{C})d\mathbf{m} = 1,\tag{2}$$

where the bold letters are vectors; A is a constant which forces $p(\mathbf{m}|\mathbf{C})$ to satisfy Eq. (2). (Since we will only use ratios of $p(\mathbf{m}|\mathbf{C})$ in MCMC simulations, the constant A will be set as 1). In terms of notation, the vertical bar "|" stands for a conditional probability. For example, $p(\mathbf{m}|\mathbf{C})$ reads the probability of m given the observation C. (Symbols used in this study are listed in Table 1.) Eq. (2) is the cumulative probability condition where the integral of the probability of **m** given the observation **C** over all **m** must be one. The prior distribution of model $\theta(\mathbf{m})$ reflects the understanding of the model before analyzing the data. In the simple cases considered in the next section where only the bounds of each model parameter are known, the prior probability θ (m) is constant within a model space restricted by those bounds. We set $\theta(\mathbf{m}) = 1$. The likelihood of observing C given model parameter m is a function of the misfit or Chi-squares, $\chi^2(\mathbf{C}, \mathbf{m})$,

$$L(\mathbf{d}|\mathbf{m}) = \exp\left(-\frac{\chi^2(\mathbf{C}, \mathbf{m})}{2}\right),\tag{3}$$

Table 1 List of key symbols.

Symbol	Description	
C, C _i	C is an array of observed multiple trace element concentrations, C_i	
$C_{ m f}$	Concentration of a trace element in the instantaneous melt	
C_s^0	Concentration of the bulk solid at the onset of melting	
d	Mineral grain size	
d_0	Reference grain size, 1.5 mm	
D	Diffusivity of the element of interest in the mineral	
D_{La}, D_{REE}	Diffusivity of La or REE in the mineral	
F	Degree of melting experienced by the bulk solid	
$F_{LS} \pm \sigma_{LS}$	The estimate of F and uncertainty obtained using the nonlinear least squares method	
$F_{MP}{}^{+\sigma_+}_{-\sigma}$	The most probable estimate of F_{MP} and asymmetric uncertainties σ_+ and σ	
$F_{mean} \pm \sigma$	The average and standard deviation of all accepted F from MCMC simulations	
f_p	Degree of melting at the onset of dynamic melting, defined in Eq. (15)	
k, k_{cpx}	Bulk solid-melt or cpx-melt partition coefficient	
k_0	Bulk solid-melt partition coefficient at the onset of melting	
k_p	Bulk solid-melt partition coefficient for the melting reaction	
$L(\mathbf{C} \mathbf{m})$	Likelihood of observing C given the model, m, defined in Eq. (3)	
m	A vector of model parameters	
$p(\mathbf{m} \mathbf{C})$	Posterior probability of a model, m, given observation C, defined in Eq. (1)	
R	The mineral-melt exchange rate constant, defined in Eq. (7)	
T_p	Potential temperature	
V_f^r, V_s	Velocity of the melt or the solid	
V_{sp}	Spreading rate	
V_0^T	Reference spreading rate, 30 mm/yr	
z	Vertical coordinate, measured from the base of the melting column	
α	The ratio between the melt and solid mass or mass flux ratio, Eq. (12)	
$\theta(\mathbf{m})$	The data-independent prior probability of the model, m	
ε	Element specific disequilibrium parameter, Eq. (5) and Eq. (16)	
$arepsilon_{La},arepsilon_{REE}$	Disequilibrium parameter for La or REE	
$arepsilon_{Tp}^0$	ε averaged along a melting path (Tp) with reference grain size and spreading rate	
ϕ_f^{ip}	Porosity	
Γ	Melting rate of the bulk solid	
ρ_f, ρ_s	Density of the melt or the solid	
$\chi^2(\mathbf{C}, \mathbf{m})$	Chi-square of observation C given the model, m	

$$\chi^{2}(\mathbf{C}, \mathbf{m}) = \sum_{i} \left(\frac{\log(C_{i}^{\text{predict}}(\mathbf{m})) - \log(C_{i})}{\sqrt{\left(\frac{\delta C_{i}^{0}}{C_{i}^{0}}\right)^{2} + \left(\frac{\delta C_{i}}{C_{i}}\right)^{2}}} \right)^{2}, \tag{4}$$

where $C_i^{\text{predict}}(\mathbf{m})$ is the concentration of element i predicted by model parameter \mathbf{m} (e.g., we can calculate $C_i^{\text{predict}}(\mathbf{m})$ as the prediction of disequilibrium fractional melting model using Eq. (6) or a more general model such as Eqs. (9)–(11) below); C_i^0 is the concentration of element i in the mantle source; δC_i^0 is the variation in the concentration of element i in the mantle source; δC_i is the uncertainty in the measured concentration of element i. Here for purpose of demonstration, we assume that the relative source variation $\delta C_i^0/C_i^0$ dominates the relative uncertainty of measurement $\delta C_i/C_i$. The posterior probability is greater if the Chi-square is smaller, i.e. the model fitting the data with smaller overall residue is more probable.

2.2. Implementation of MCMC through the Metropolis—Hastings algorithm

To obtain the posterior distribution defined by Eqs. (1)-(4), we carry out MCMC simulations using the

Metropolis-Hastings algorithm that consists of the following steps (Hastings, 1970; Sambridge and Mosegaard, 2002; Robert and Casella, 2004; Liu, 2008):

- Step 1. Start from any model $\mathbf{m_0}$. Calculate predicted observation $\mathbf{C}^{\text{predict}}(\mathbf{m_0})$. Calculate the likelihood function $L(\mathbf{m_0}|\mathbf{C})$ according to Eqs. (3) and (4).
- Step 2. Suppose $\mathbf{m_k}$ is the current model (if this step follows Step 1, k = 0). Choose a temporary model $\mathbf{m_{temp}}$ randomly. Calculate predicted observation $\mathbf{C^{predict}}(\mathbf{m_{temp}})$. Calculate the likelihood function $L(\mathbf{m_{temp}}|\mathbf{C})$ according to Eqs. (3) and (4).
 - if the ratio $p(\mathbf{m_{temp}}|\mathbf{C}) / p(\mathbf{m_k}|\mathbf{C}) > 1$, accept $\mathbf{m_{temp}}$ as $\mathbf{m_{k+1}}$.
 - else, generate a uniformly distributed random number, t, between 0 and 1.
 - o if $p(\mathbf{m_{temp}}|\mathbf{C})/p(\mathbf{m_k}|\mathbf{C}) > t$ or the iteration of Step 2 has reached a pre-defined maximum number (2000 in this study), accept $\mathbf{m_{temp}}$ as $\mathbf{m_{k+1}}$.
 - o else, go to Step 2.
- Step 3. Continue to Step 2 until a sufficient number of accepted models are produced.

The set of accepted models converges to the posterior distribution after sufficient numbers of models are collected. However, the exact number can only be determined empirically. In this study, we use the Metropolis–Hastings algorithm to acquire a sample set consisting of at least 1000 accepted models. There are alternative algorithms to implement MCMC simulations (Robert and Casella, 2004; Liu, 2008). For example, "Gibbs Sampling", which, in its basic form is a special case of the Metropolis–Hastings algorithm, is more desirable for models with a large number of parameters. Korenaga and Karato (2008) recently used the Gibbs sampling to analyze experimental data on olivine rheology.

The result of MCMC simulations following the procedure outlined in the preceding section is a set of accepted models $(\mathbf{m_0}, \mathbf{m_1}, \dots, \mathbf{m_n})$ representing the posterior distribution of model parameters, e.g., F and ε in the case of disequilibrium fractional melting. Among these models, there is one model called "the most probable model" whose probability in reproducing the observed data is the greatest, designated as $\mathbf{m_{MP}} = (F_{\mathrm{MP}}, \, \varepsilon_{MP})$ or $(F_{\mathrm{MP}}, \, \varepsilon_{MP}, \, \alpha_{\mathrm{MP}})$ for the two melting models considered in the next section. In general, the probability distribution of F is not normal or symmetric. To facilitate comparison with normal distribution, we use σ_{-} and σ_{+} as lower and upper standard deviation of F. The probability that an F randomly chosen from $(F_0, F_1, \ldots, F_n, \text{ where } F_i \text{ belongs to } \mathbf{m_i})$ falls into the interval $[F_{\mathrm{MP}}-\sigma_{-},F_{\mathrm{MP}}+\sigma_{+}]$ is 68%. The procedure for finding σ_{-} and σ_+ is presented in Appendix A. For convenience, we use the notation $F_{MP}^{+\sigma_+}_{-\sigma_-}$ to describe the most probable model of F with non-normal posterior distribution. We use this notation for all parameters in the model. In the special case of normal distribution, $\sigma_{-} = \sigma_{+}$. We recover the mean and standard deviation of F, viz., $F_{mean} \pm \sigma$.

As for the nonlinear least squares method, the estimate of a model parameter, say F, has a symmetric form because the method implicitly assumes a normal distribution of F characterized by the mean (F_{LS}) and the standard deviation (σ_{LS}) . Since the nonlinear least squares method proceeds through iteration to find F_{LS} which fits the data with the smallest overall residue, F_{LS} is expected to be the same as F_{MP} if the iteration converges. The standard deviation obtained by the nonlinear least squares method does not have to be the same as σ_- or σ_+ unless the posterior distribution is normal. We will compare results in these three formats $(F_{MP}^{+}_{-\sigma_+}, F_{mean} \pm \sigma, \text{ and } F_{LS} \pm \sigma_{LS})$ in a case study in Section 3.2.

3. CASE STUDIES

3.1. Data and source composition

To demonstrate the advantages of the MCMC method, we consider REE and Y abundances in clinopyroxene (cpx) in abyssal peridotites from several mid-ocean ridges. To focus on melting history, we consider residual lherzolites and harzburgites that show no obvious signs of mantle metasomatism or late stage melt refertilization (i.e., presence of interstitial plagioclase, cross-cutting veins or amphi-

bole; LREE enrichment in cpx; high TiO₂ (>1 wt%) in spinel, Warren, 2016; see Section 5.3 for additional discussion). We further choose samples with at least 8 reported trace elements (REE and Y) in cpx. This procedure leads to a data set of 135 samples (Table 2, data from Johnson et al., 1990; Hellebrand et al., 2002; Salters and Dick, 2002; Hellebrand and Snow, 2003; Brunelli et al., 2006; Brunelli and Seyler, 2010; Lassiter et al., 2014; Mallick et al., 2014). Following Liang and Liu (2016), we exclude La in our data if the chondrite-normalized ratio (La/Ce)_N is too high to be explained by a melting model alone. The melting history of each sample is recorded by multiple incompatible trace element abundances in cpx. Concentrations of the selected trace elements in cpx will be regarded as a data vector C in MCMC simulations as described in Section 2. We recognize that trace element and isotope compositions of mantle sources beneath mid-ocean ridge spreading centers vary among different ridge systems. For simplicity, we consider melting of the depleted MORB mantle or DMM (Workman and Hart, 2005) in the spinel peridotite field. Liang and Peng (2008) examined the role of garnet field melting and concluded that it is not needed to explain the observed REE patterns in cpx in abyssal peridotites from the Central Indian Ridge (Hellebrand et al., 2002). We consider two disequilibrium melting models: one with an analytical solution and the other without. The former allows us to compare with results from direct nonlinear least squares inversion (Liang and Liu, 2016). The latter melting model is more general as it has one additional model parameter. Our goal in this section is to demonstrate the procedure and advantage of MCMC method through two case studies of a subset of data from the Central Indian Ridge. In Section 4, we further expand case study two by considering trace element data from other mid-ocean ridge systems listed in Table 2.

3.2. Case study one: melting model with an explicit analytical solution

Disequilibrium melting happens when diffusion in residual minerals for a trace element of interest cannot keep up with melting of the minerals. It can be characterized by a disequilibrium parameter ε which is defined as the ratio of melting rate relative to chemical exchange rate,

$$\varepsilon = \frac{\Gamma}{\rho_s (1 - \phi_f) R},\tag{5}$$

where Γ and ρ_s are the melting rate and density of the bulk solid, respectively; ϕ_f is the porosity; and R is the exchange rate constant. During disequilibrium fractional melting, the concentration of a trace element in residual cpx, $C(\mathbf{m})$, varies as a function of F and ε , and is given by the simple expression (Liang and Liu, 2016),

$$C(\mathbf{m}) = C_s^0 \frac{k_{cpx}}{k_0} \left(1 - \frac{\varepsilon + k_p}{\varepsilon + k_0} F \right)^{\frac{1 - k_p}{k_p + \varepsilon}}, \tag{6}$$

where C_s^0 is the concentration of the trace element in the mantle source; k_0 is the bulk partition coefficient at the onset of melting; k_p is the bulk partition coefficient

Table 2 List of sample locations and sources.

Sample location	Number of samples	Data sources
Southwest Indian Ridge (SWIR)	35	Salters and Dick (2002); Warren (2007); Seyler et al. (2011); Mallick et al. (2014)
Lena Trough (LT) at Arctic Ridge	25	Hellebrand and Snow (2003), Lassiter et al. (2014)
American-Antarctic Ridge (AAR)	9	Johnson et al. (1990)
Vema Lithospheric Section (VLS) at Mid-Atlantic Ridge	35	Brunelli et al. (2006)
Kane FZ & St. Paul FZ (KSP) at Mid-Atlantic Ridge	9	Brunelli and Seyler (2010), Mallick et al. (2014)
Central Indian Ridge (CIR)	22	Hellebrand et al. (2002)

calculated according to melting reaction; and k_{cpx} is the cpx-melt partition coefficient. Eq. (6) reduces to the familiar equilibrium non-modal perfect fractional melting model when $\varepsilon = 0$. For diffusion in solid limited mass transfer, the exchange rate constant R is inversely proportional to the diffusion time scale in the mineral. For spherical grain of radius d, R is given by (e.g., Navon and Stolper, 1987; Bodinier et al., 1990),

$$R = \frac{15D}{d^2},\tag{7}$$

where *D* is the diffusivity of the element of interest in the mineral.

A key assumption used to derive Eq. (6) is that the mineral-melt exchange rate constants are the same for all the minerals. For modeling REE fractionation during disequilibrium melting of spinel peridotite, Liang and Liu (2016) demonstrated that it is reasonable to use REE diffusion coefficients in cpx to calculate R. Since the disequilibrium parameter of a REE (ε_{REE}) is inversely proportional to its diffusion coefficient (Eqs. (5) and (7)), it is convenient to scale ε_{REE} for REE and Y to that of La (designated as ε_{La} hereafter) according to their diffusion coefficients in cpx (diffusivity data from Van Orman et al., 2002), viz.,

$$\varepsilon_{REE} = \frac{D_{La}}{D_{REE}} \varepsilon_{La}. \tag{8}$$

Liang and Liu (2016) used Eqs. (6) and (8) and a nonlinear least squares method to invert for F and ε_{La} from REE and Y abundances in cpx in 22 abyssal peridotites from the Central Indian Ridge (CIR, Hellebrand et al., 2002). To compare with their results and to test the new inversion method, here we conduct MCMC simulations for the 22 samples from CIR using the same mineral-melt partition coefficients, diffusion coefficients, melting reaction, and starting mantle composition as in their study. For shorthand notation, we set $\varepsilon = \varepsilon_{La}$ hereafter. Hence, the model in MCMC simulations has two unknown parameters: degree of melting and extent of disequilibrium for La in cpx, designated as $\mathbf{m} = (F, \varepsilon)$.

We choose the prior distribution as a uniform distribution in a two-dimensional model space. In other words, any $\mathbf{m} = (F, \varepsilon)$ in the model space has the same prior probability. The bound for F is less than the degree of melting when cpx is exhausted (F < 18%, Baker and Stolper, 1994). The bound for ε is [0, 0.05] according to previous

inversion results (Liang and Liu, 2016). Fig. 1 displays results of 6231 MCMC simulations for sample ANTP126-2 following the steps outlined in Section 2.2. Here the observed data are shown as yellow circles and each gray line represents an REE pattern calculated using accepted m from MCMC simulations. Those REE patterns predicted by models within the asymmetric confidence interval $([F_{MP} - \sigma_{-}, F_{MP} + \sigma_{+}] \text{ and } [\varepsilon_{MP} - \sigma_{-}, \varepsilon_{MP} + \sigma_{+}]) \text{ define}$ a region enclosing the data (Fig. 1). The prediction with the most probable model is the best fit to the data (red line in Fig. 1). Figs. 2a and 2b display marginal distributions of F and ε , respectively. The marginal distribution of ε is skewed: σ_+ of ε is larger than σ_- of ε . The normal distribution derived from nonlinear least squares inversion is markedly narrower than the accepted models from MCMC simulations in the histogram. The discrepancy between sample mean and the most probable model also indicates asymmetry of posterior distribution of ε . In a plot of ε vs.

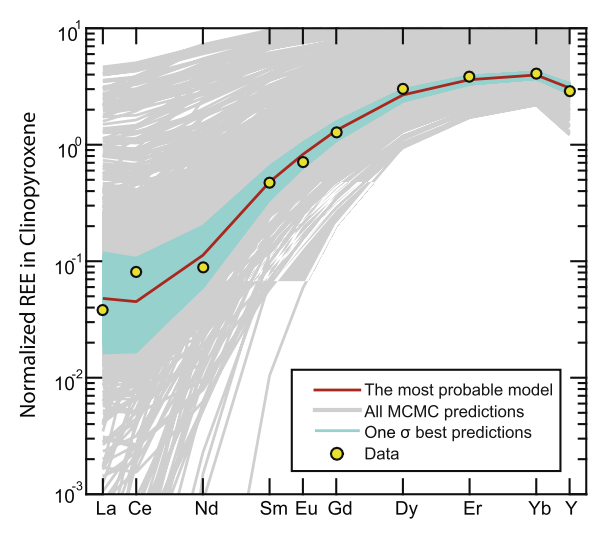


Fig. 1. Comparison between observed (circles) and model derived (lines) REE+Y patterns in residual clinopyroxene in spinel lherzolite. The observed data are from an abyssal peridotite from the Central Indian Ridge (Hellebrand et al., 2002, their sample ANTP126-2). Individual lines are calculated using the disequilibrium fractional melting model (Eq. (6)) through MCMC simulations. Concentrations in clinopyroxene are normalized by CI chondrite (Anders and Grevesse, 1989).

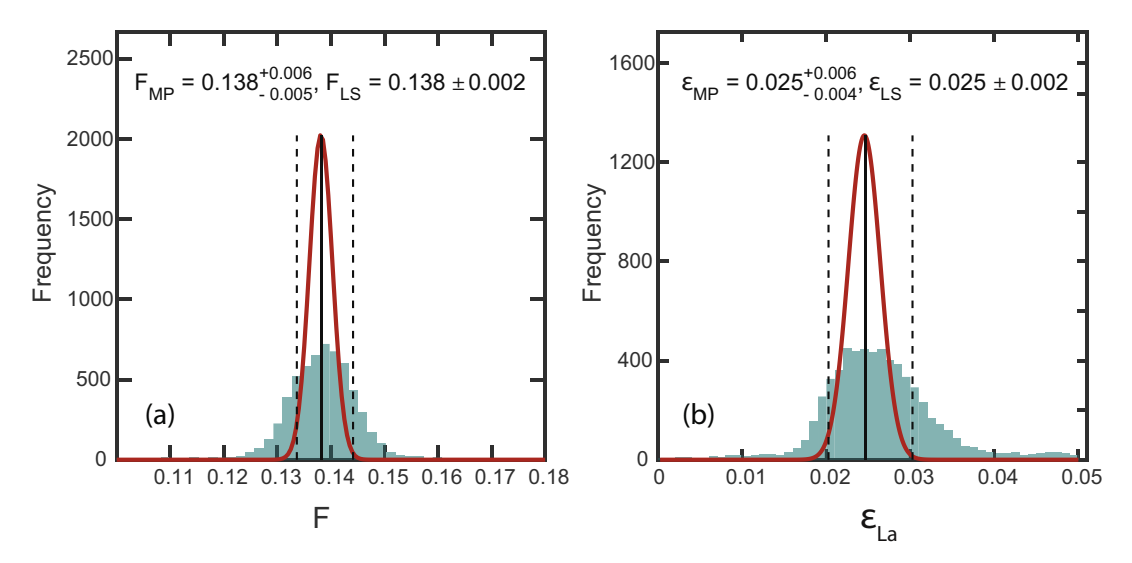


Fig. 2. Histograms displaying MCMC simulation results of sample ANTP126-2 for the degree of melting (F, panel a) and the disequilibrium parameter for La in clinopyroxene (ε_{La} , panel b) obtained using the disequilibrium fractional melting model (Eq. (6)). Black solid line in each panel marks the most probable model. Black dashed lines are the upper and lower σ about the most probable model. Red curves correspond to the normal distribution based on nonlinear least squares inversion. (For interpretation of the references to colour in this figure legend, the reader is referred to the web version of this article.)

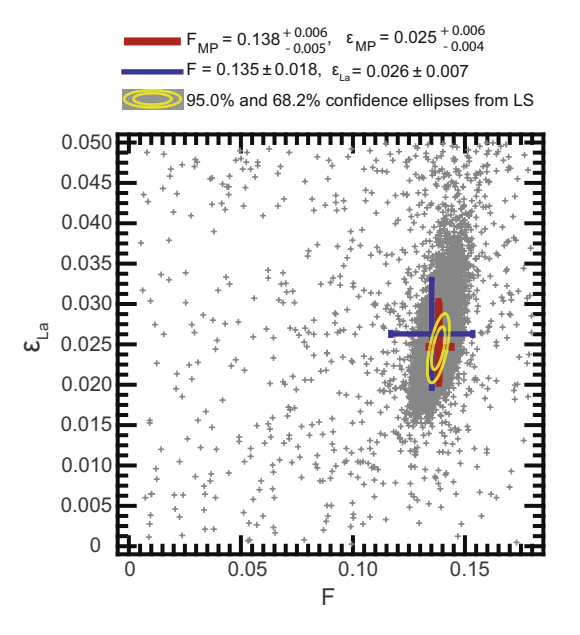


Fig. 3. Plot of accepted model parameters for sample ANTP126-2 in F- ε_{La} plane. Red error bars correspond to the most probable model with upper/lower σ . Blue error bars correspond to mean $\pm \sigma$. Also shown are results from nonlinear least squares inversion (ellipses). The larger ellipse corresponds to 95% confidence level, while the smaller ellipse corresponds to 68.2% confidence level. The 68.2% confidence eclipse underestimates the uncertainties of F and ε for La in clinopyroxene. (For interpretation of the references to colour in this figure legend, the reader is referred to the web version of this article.)

F, accepted models scatter around a near elliptical figure centered at the most probable model (Fig. 3). Positive trade-off between F and ε is demonstrated by the NE-SW trend of the accepted models. The ranges of asymmetric

uncertainty estimate (σ_+ and σ_-) are larger than or comparable to the 68% confidence ellipse for normal distribution. Figures similar to Figs. 1–3 for the 22 CIR samples are presented in Supplementary Fig. S1. For a few samples, the uncertainty range characterized by σ_+ and σ_- is greater than the range of 95% confidence ellipse derived from direct nonlinear least squares inversion (samples ANTP87-5, ANTP87-9, ANTP89-2, ANTP89-5, ANTP89-8, and ANTP89-15). The nonlinear least squares method cannot describe asymmetric probability distribution of ε and may lead to underestimate of uncertainty.

The most probable model derived from MCMC simulations is not necessarily a good fit to the data. The most probable model still cannot fit sample CIRCE93-7 which exhibits a "hump shape" REE pattern. Here the probability of the most probable model is effectively zero $(p=1\times10^{-14}~\rm according$ to Eqs. (1)–(4)), which means that the melting model (Eq. (6)) cannot explain this sample. A more general model involving refertilization by a small amount of melt produced in the lower part of the melting column, as suggested by Hellebrand et al. (2002), can explain the observed REE data. To avoid samples affected by refertilization and other post-melting processes (discussed in Section 5.3), any sample that has the probability less than 1×10^{-4} for the most probable model is excluded in this case study.

For all samples, the model estimates from nonlinear least squares inversion are consistent with those derived from the most probable model (Fig. 4). But the means of accepted models show systematic deviation from the most probable model and the nonlinear least squares results (Fig. 4). For $F_{MP} > 15\%$, F_{mean} is smaller than F_{MP} and F_{LS} , whereas for $F_{MP} < 15\%$, ε_{mean} is greater than ε_{MP} and ε_{LS} . Since the model represents the most probable physical condition given the data constraint, we recommend using F_{MP} over F_{mean} . For later discussion,

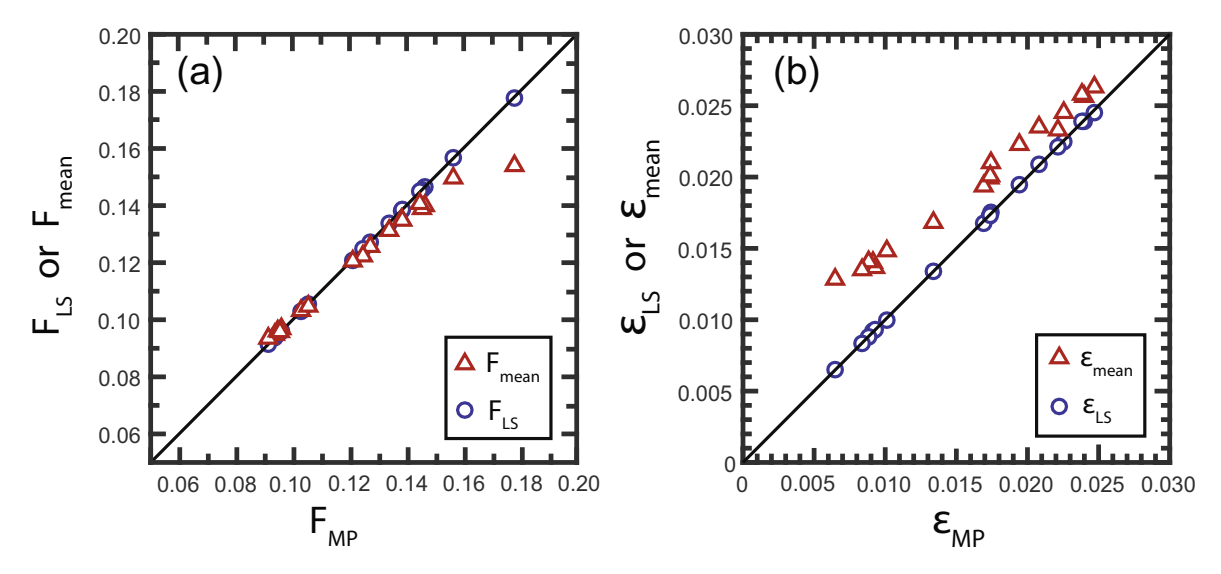


Fig. 4. Comparison of melting parameters derived from MCMC simulations and nonlinear least squares inversions of REE + Y in residual clinopyroxenes in abyssal peridotites from the Central Indian Ridge (data from Hellebrand et al., 2002). (a) Degree of melting (F). (b) ε_{La} , disequilibrium parameter for La in clinopyroxene. Subscripts 'MP' and 'LS' refer to the most probable model parameter from MCMC simulations and nonlinear least squares method. See text for discussion.

the estimate of the model parameter will be presented in the asymmetric form, $F_{MP}^{+\sigma_+}_{-\sigma_-}$ and $\varepsilon_{MP}^{+\sigma_+}_{-\sigma_-}$.

3.3. Case study two: melting model without explicit analytical solution

The preceding example demonstrates the procedure of MCMC method and its advantage in estimating meaningful uncertainties for model parameters. In this section, we show another important advantage of MCMC method using a disequilibrium dynamic melting model that does not have an explicit analytical solution. Nonlinear least squares inversion of such a problem is challenging, if not impossible. Here we show that MCMC simulation is well suited for this class of inverse problems.

The dynamic or continuous melting model has been widely used to study trace element fractionation during mantle melting (e.g., Langmuir et al., 1977; McKenzie, 1985; Zou, 1998; Shaw, 2000). Here we consider a more general case of dynamic melting by allowing chemical disequilibrium between residual minerals and interstitial melt. In nondimensional form, the governing mass conservation equations for a trace element in the interstitial melt (C_f) and residual solid (C_s) are given by two coupled ordinary differential equations (a derivation is presented in Appendix B). In terms of the degree of melting, we have

$$(1 - F)\varepsilon\alpha \frac{dC_f}{dF} = \varepsilon(C_s^p - C_f) + (C_s - kC_f), \tag{9}$$

$$(1-F)\varepsilon \frac{dC_s}{dF} = -\varepsilon (C_s^p - C_s) - (C_s - kC_f), \tag{10}$$

$$(1-F)\varepsilon \frac{dC_s^j}{dz} = -(C_s^j - k_j C_f), \tag{11}$$

$$\alpha = \frac{\rho_f \phi_f V_f}{\rho_s (1 - \phi_s) V_s},\tag{12}$$

where ε is defined by Eq. (5); α is the mass flux ratio between the melt and the residual solid; C_s^p is the concentration of bulk solid calculated according to melting reaction (Eq. (B5) in Appendix B); k is the bulk partition coefficient (Eq. (B6)); V_f is the velocity of the melt; and V_s is the upwelling velocity of the solid matrix. To be consistent with equilibrium dynamic melting models of Zou (1998) and Shaw (2000), we assume that dynamic melting starts at $F = f_p$ before which melting takes place as equilibrium batch melting. Hence the initial melt and solid compositions at $F = f_p$ are

$$C_f = \frac{C_s^0}{k_0 + (1 - k_P)f_n},\tag{13}$$

$$C_s = \frac{C_s^0}{k_0 + (1 - k_P)f_p} \frac{k_0 - k_P f_p}{1 - f_p},\tag{14}$$

where f_p is related to α through the simple expression (Shaw, 2000),

$$f_p = \frac{\alpha}{1+\alpha}.\tag{15}$$

The disequilibrium dynamic melting model has three parameters (F, ε, α) . It recovers the equilibrium dynamic melting when $\varepsilon=0$, the disequilibrium perfect fractional melting when $\alpha=0$. For an incompatible trace element, its concentration in residue at a given F increases with α or ε (Liang and Liu, 2016). Since there is no explicit analytical solution to Eqs. (9)–(11), here we invert the melting parameters through MCMC simulations. Our observations include REE and Y abundances in cpx in the 22 abyssal peridotites from CIR. We solve Eqs. (9)–(11) numerically using the third-order Runge Kutta method (Shu and Osher, 1988), starting from the initial conditions prescribed by Eqs. (13) and (14).

The prior bounds for model parameters are $f_p < F < 0.18$, $0.0002 < \varepsilon < 0.05$, and $0.0005 < \alpha < 0.04$. The upper bound for F and ε are the same as in case study one. The lower bound for F is the onset of dynamic melting (Eq. (15)). The upper bound for α is equivalent to a scenario in which there is 2% porosity and the melt percolates two times faster than the solid. The non-zero lower bounds for ε and α are for the consideration of numerical stability in solving Eqs. (9)–(11). These upper and lower bounds are conservative with respect to the most probable models.

Fig. 5 shows results of MCMC simulations for three samples: one with effectively zero α (ANTP126-2), one with effectively zero ϵ (ANTP89-1), and one with intermediate α and ϵ (sample CIRCE93-4). These model parameters are not from normal distributions. Fig. 6 displays the asymmetric marginal distributions of F, ϵ , and α for sample ANTP126-2. The most probable model deviates from the peak of marginal distribution as a result of 3D to 1D projection. This is further illustrated in Fig. 7 for the three samples displayed in Fig. 5. Even when projected on F- ϵ

and ε - α planes, accepted models as points of **m** = (F, ε , α) clearly display nonlinear trade-offs. There is a broad negative correlation between ε and α in Figs. 7b, 7e and 7h. The distribution near the origin on the ε - α plane is considerably sparser than the region where α and ε are greater than 0.01 (Fig. 7b). Thus, equilibrium fractional melting is unlikely for sample ANTP126-2. Further, the ε - α correlation is not characterized by an ellipse expected in a bimodal normal distribution. The probability distribution is denser near the ε axis than near the α axis (Fig. 7b). The most probable model has small α and relatively large ε , which is clearly shown in Fig. 7c. Therefore, sample ANTP126-2 is better represented by a model that is closer to disequilibrium fractional melting than equilibrium dynamic melting. (The converse is true for sample 89–1.) Figs. 7d–7f are from a model with both ε and α greater than 0.01, an intermediate case that cannot be represented by known analytical solutions (i.e., disequilibrium factional melting model ($\alpha = 0, \ \epsilon > 0$) or equilibrium dynamic melting model ($\varepsilon = 0, \alpha > 0$)). The estimate of ε in case study one only considers the $\alpha = 0$

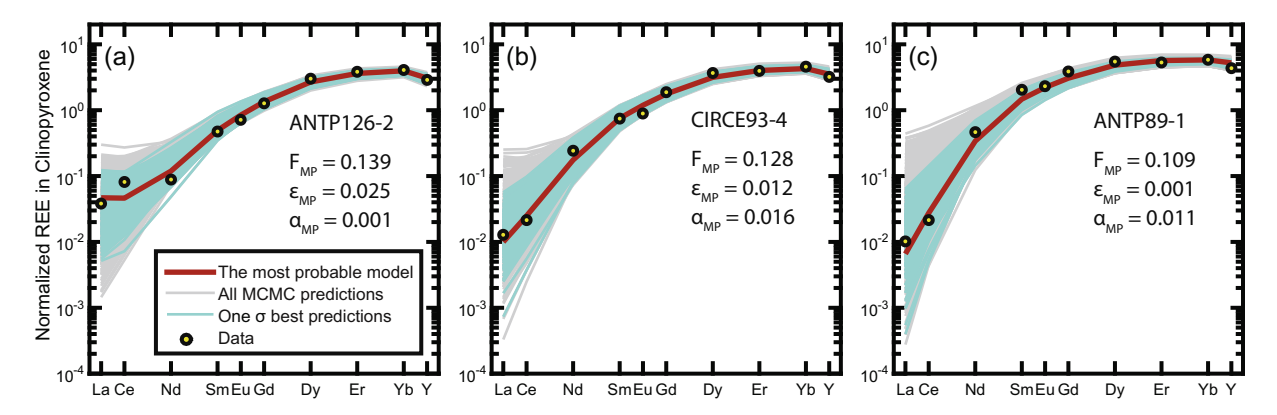


Fig. 5. Comparison between observed (circles) and model derived REE + Y patterns in clinopyroxene in abyssal peridotites. Three samples from the Central Indian Ridge (Hellebrand et al., 2002) are shown as examples of disequilibrium fractional melting (a), disequilibrium dynamic melting (b), and equilibrium dynamic melting (c). Individual curves are calculated using the disequilibrium dynamic melting model (Eqs. (9)–(11)) through MCMC simulations. Parameters for the most probable model are listed in each panel. See text for discussion.

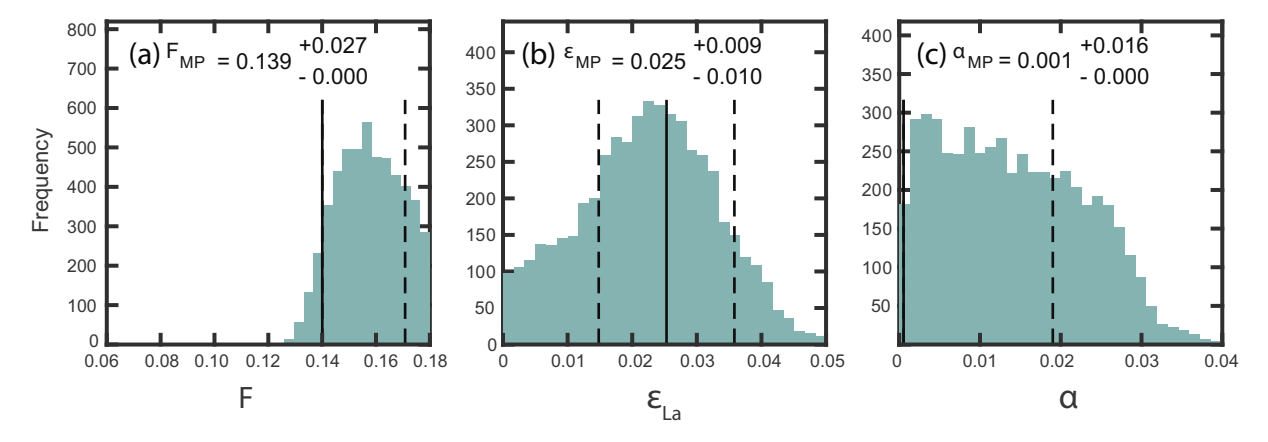


Fig. 6. Histograms displaying MCMC simulation results of sample ANTP126-2 for the degree of melting (F, panel a), the disequilibrium parameter for La in clinopyroxene (ε_{La} , panel b), and the mass flux ratio or fraction of melt retained (α , panel c) obtained using the disequilibrium dynamic melting model (Eqs. (9)–(11)). Solid line in each panel represents the most probable model. Dashed lines mark uncertainty interval about the most probable model. Notice the most probable model parameter may lie on the boundary of uncertainty interval.

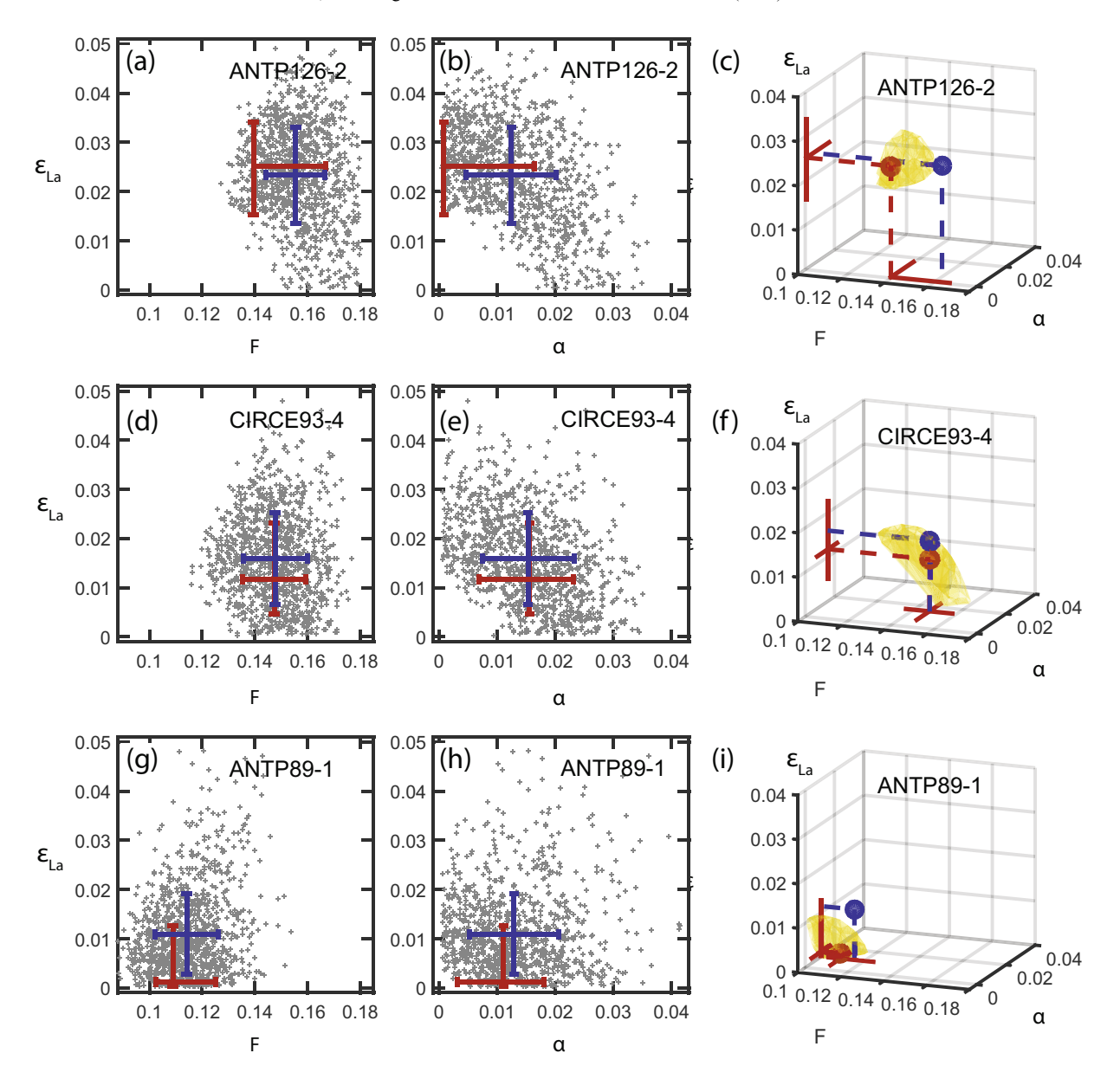


Fig. 7. Plots of accepted model parameters for three samples in F- ε_{La} plane (a, d, g), ε_{La} - α plane (b, e, h), and F- ε_{La} - α space (c, f, i). Model parameters are derived from MCMC simulations using the disequilibrium dynamic melting model (Eqs. (9)–(11)). Red error bars correspond to the most probable model with upper/lower σ . Blue error bars correspond to the symmetric format of mean $\pm \sigma$. The gold shade regions in the 3D space mark the ranges of 10% best models. (For interpretation of the references to colour in this figure legend, the reader is referred to the web version of this article.)

plane in F- ε - α space. Because there exist trade-offs between ε and α , case study one would overestimate ε . The trade-off between the extent of disequilibrium and the extent of incomplete melt extraction has been noted in previous studies (Qin, 1992; Iwamori, 1993a,b; Van Orman et al., 2002). The preceding examples demonstrate that with MCMC simulations it is possible to target the most probable combination of ε and α for an individual sample. Similar figures summarizing MCMC simulations for all the samples included in this study are presented in Supplementary Fig. S2. Melting parameters from the most probable model are summarized in Supplementary Table S1.

Fig. 8 compares results from case studies one and two for the CIR samples. In general, ε estimated in case study two (unfilled circles) are smaller, especially for those samples with F less than 13%. This is largely due to the negative trade-off between ε and α in the disequilibrium dynamic melting model, i.e., the product $\varepsilon \alpha$ in Eq. (9). The lower values of ε in the disequilibrium dynamic melting model are compensated by α which is absent in the disequilibrium perfect fractional melting model. (For the same reason, values of α derived from the equilibrium dynamic melting model would be higher than values obtained from the disequilibrium dynamic melting model.) Therefore, values of ε

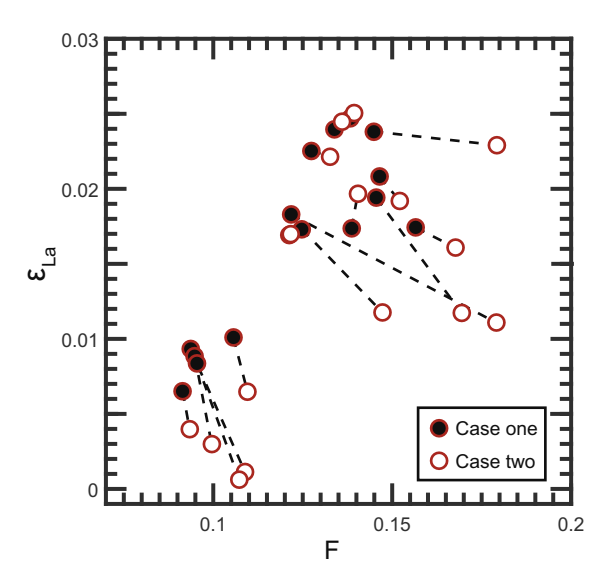


Fig. 8. Comparison of the most probable parameters (F and ε_{La}) derived from MCMC simulations using the disequilibrium perfect fractional melting model (Eq. (6)) and the disequilibrium dynamic melting model (Eqs. (9)–(11)) for samples from the Central Indian Ridge in the two case studies discussed in Section 3. Results for a given sample from the two case studies are connected by a dashed line. The disequilibrium fractional melting model in case one overestimates ε when F is smaller than 13%.

derived from the more general melting model in case study two are more reliable than values derived from the disequilibrium fractional melting model in case study one and the equilibrium dynamic melting model.

4. APPLICATION TO ABYSSAL PERIDOTITES FROM OTHER SELECTED MID-OCEAN RIDGE SYSTEMS

One of the major motivations for our MCMC study is the positive correlation between F and ε derived from nonlinear least squares inversion of REE and Y abundances in cpx in abyssal peridotites from CIR using the disequilibrium fractional melting model (Liang and Liu, 2016). This positive correlation is further confirmed in the present study through the application of the more general disequilibrium dynamic melting model (Figs. 8 and 9d). An interesting question is if similar correlation between F and ε also exists in abyssal peridotites from other mid-ocean ridge systems. In this section, we expand case study two to include peridotites from the Vema Lithospheric Section (VLS, 35 samples, Brunelli et al., 2006), Kane Fracture Zone and Saint Paul Fracture Zone (KSP, 9 samples, Brunelli and Seyler, 2010; Mallick et al., 2014) at the Mid-Atlantic Ridge, the South West Indian Ridge (SWIR, 35 samples, Salters and Dick, 2002; Warren, 2007; Seyler et al., 2011; Mallick et al., 2014), Lena Trough at the Arctic Ocean (LT, 25 samples, Hellebrand and Snow, 2003; Lassiter et al., 2014), and the American-Antarctica Ridge (AAR, 9 samples, Johnson et al., 1990). The spreading rates of SWIR, LT, and AAR (<20 mm/yr) are slower than CIR (30–51 mm/yr), while the spreading rates of VLS and KSP at Mid-Atlantic Ridge (25–31 mm/yr) are at the lower end of CIR (Argus and Gordon, 1991; DeMets et al., 2010).

Supplementary Table S1 summarizes results from MCMC simulations based on the disequilibrium dynamic melting model (Eqs. (9)–(15)). Supplementary Fig. S2 present MCMC simulations of individual samples. Similar to case study one, samples with poor fit are excluded according to a threshold probability. As a result of this filtering, thirty-four out of 135 samples are disqualified. REE abundances in these samples are likely affected by secondary processes such as melt refertilization (see Section 5.3 for additional discussion). As a precaution, we exclude these samples in the interpretation of the disequilibrium dynamic melting model. If we only consider the most probable model, samples from all mid-ocean ridge systems considered in this study except two from SWIR (samples EDUL-6B-1-3 and EDUL-23-2-8 from Seyler et al., 2011) show a positive correlation between F and ε for La, although the range of variation differs among localities (Fig. 9). The lower bound of ε for these two samples still lie on the trend of the rest of 25 samples from SWIR (magenta squares in Fig. 9a). A model on the F–ε trend still produces an acceptable fit (Figs. 9 and S2). Samples from SWIR and CIR show strong positive trends even when uncertainties are considered (Fig. 9a and d).

5. DISCUSSION

5.1. The positive correlation between F and ε

We have demonstrated in the preceding sections that the positive correlations between F and ε for La in cpx in abyssal peridotites is a robust feature of mantle melting beneath mid-ocean ridge spreading centers. The disequilibrium parameter ε is defined as the ratio of the melting rate to the solid-melt diffusive exchange rate for La in cpx (Eq. (5)). The melting rate is proportional to solid upwelling rate (V_s) and melt productivity (dF/dz) along the melting column. The diffusive exchange rate is inversely proportional to the time scale of La diffusion in cpx (Eq. (8)). Liang and Liu (2016) presented a simple equation relating ε to these parameters for a steady-state melting column, viz.,

$$\varepsilon_{La} = \frac{V_s d^2}{15(1-F)D_{La}} \frac{dF}{dz},\tag{16}$$

where D_{La} is the diffusivity of the trace element of interest (La) in cpx. In the calculation below, we take V_s as half of the local spreading rate (Argus and Gordon, 1991; DeMets et al., 2010). The disequilibrium parameter ε is very sensitive to cpx grain size (Eq. (16)). There are considerable uncertainties in cpx grain size and its size distribution in the starting mantle. Since our goal here is to understand the positive correlation between F and ε , we compare melting models with the same cpx grain size at the onset of melting (d=1.5 mm). Furthermore, we assume that the average grain size of cpx decreases in proportion to cpx volume reduction during melting.

Asimow et al. (1997, 2001) demonstrated that one can use the thermodynamic model MELTS to calculate melt productivity along a melting column. Fig. 10 displays

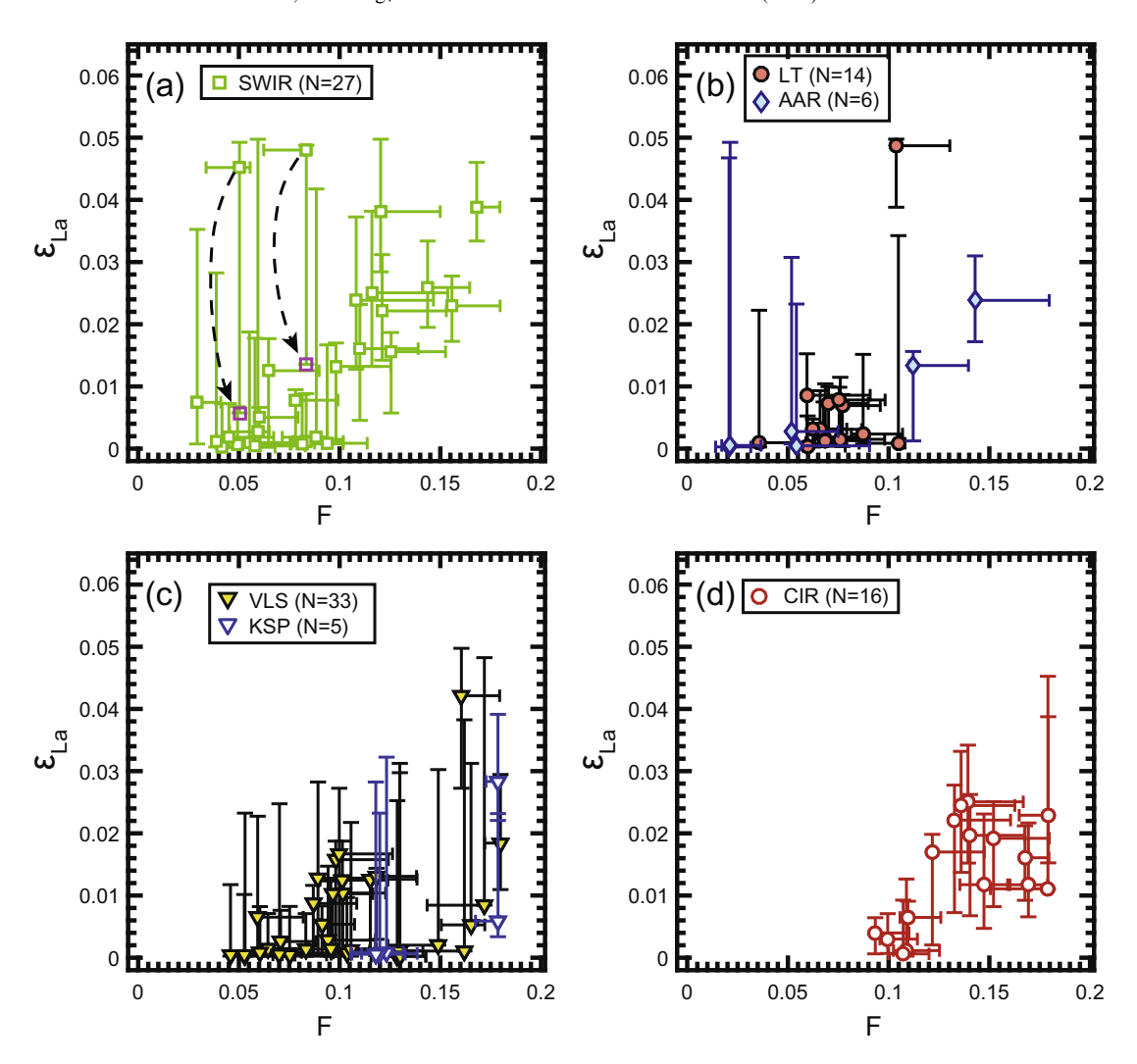


Fig. 9. Plots of inverted F and the disequilibrium parameter ε_{La} for samples from selected ridges (see Table 2 for data source). The arrows and magenta squares in (a) suggest models closer to the main trend can explain these two samples. (The REE pattern derived from the on-trend model can be found in Supplementary Fig. S2). Samples from SWIR and CIR show robust positive trends. N is the number of samples from a given ridge system. (For interpretation of the references to colour in this figure legend, the reader is referred to the web version of this article.)

calculated disequilibrium parameters for La (ε_{La}) along three melting paths using pMELTS (Ghiorso et al., 2002; Smith and Asimow, 2005) for anhydrous melting of a DMM source (Workman and Hart, 2005). The calculated ε_{La} is smaller for higher potential temperature as a result of strong temperature dependent diffusivity. The disequilibrium parameter ε_{La} varies by one order of magnitude over the range of potential temperatures considered (1280-1340 °C). The increase of ε_{La} at lower F is due to increasing melt productivity and decreasing diffusion rate, while the decrease of ε_{La} at higher F is due to grain size reduction of cpx during melting. The latter is not well constrained. In a more realistic case where cpx has a range of grain size in the starting mantle, it is possible that smaller cpx grains will be preferentially consumed earlier during melting than larger grains. Hence the decrease in predicted ε_{La} along a given mantle adiabat may be less than that shown in Fig. 10 for uniform cpx grain size distribution at higher degrees of melting (e.g., F > 14%). In case study two, we assume ε_{La} to be constant along the melting column. Thus the inverted ε should be regarded as an average value during disequilibrium melting. For comparison, we also calculate the average of ε_{La} at a given F as the arithmetic mean of ε_{La} from the onset of melting to F. Fig. 10 shows that the average ε_{La} (dashed lines) increases but lags behind the instantaneous ε_{La} at lower F. As F further increases, the average ε_{La} levels off. In spite of uncertainties in cpx grain size, grain size variation and distribution, the positive correlations between the inverted ε and F shown in Figs. 9a–9d are consistent with the predicted correlation between ε_{La} and F at a given mantle potential temperature (Fig. 10).

5.2. Variation of ε at a given F

There are considerable variations of ε for La at a given F among samples from the same ridge segments and between samples from different ridges (Fig. 9). Possible factors responsible for the observed variations of ε_{La} at a given F include, but are not limited to (see Section 5.3 below), grain

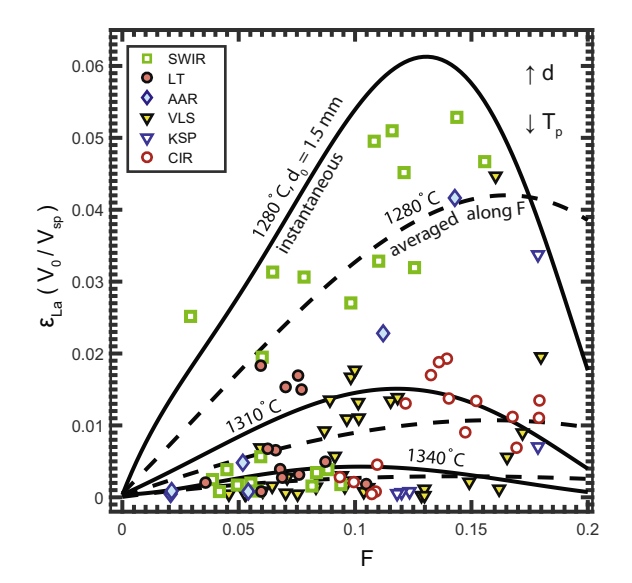


Fig. 10. Variations of the calculated disequilibrium parameter ε_{La} as a function of F along three adiabat melting paths (solid curves). Dashed lines are arithmetic average of ε_{La} from the onset of melting to F. In general, ε_{La} increases with initial grain size (d) and decreases with potential temperature (T_p) . To facilitate comparison, we renormalize ε_{La} from different ridges (symbols) to a reference spreading rate of $V_0 = 30$ mm/yr. See text for discussion.

size variation among segments, grain size distribution in a single segment, upwelling rate, and potential temperature. In the following discussion, "variation in ε " refers to "variations of ε at a given F" unless stated otherwise. We first consider variations of ε among different ridge segments by normalizing inverted data shown in Fig. 9 with respect to the upwelling rate.

According to Eq. (16), ε_{La} is proportional to local upwelling rate (and hence spreading rate). Thus the inverted ε from ridges of different spreading rate are not directly comparable. To facilitate comparison, we renormalize ε from different ridges to a common or reference

spreading rate V_0 (=30 mm/yr). The results are shown in Fig. 10. If the variation in ε is due to upwelling rate alone, Fig. 10 would plot all scaled inversion results on the same trend. But this is not the case. High ε and low F is common for samples from ridges with ultra-slow spreading rate (SWIR, LT, and AAR), while ridges with intermediate spreading rate (CIR) show lower ε and higher F. Two data sets from the slow spreading Mid-Atlantic Ridge (VLS and KSP) plot between CIR and ultra-slow spreading ridges. This is further illustrated in Fig. 11b where samples with large ε/F ratios are from ultra-slow spreading ridges (SWIR, LT, AAR), while samples with small ε/F ratios are from intermediate-slow spreading ridges (CIR).

Different local F- ε trends suggest factors other than upwelling rate contribute to the bulk of the variation in ε . In general, ε/F increases with grain size and decreases with potential temperature. A reduction of potential temperature from 1310 °C to 1280 °C can explain the threefold variation in ε at a given F (Fig. 10). If the average ε/F is due to potential temperature while the scatter is due to grain size variation, the negative trend of ε/F vs. spreading rate in Fig. 11 could be understood in terms of a positive correlation between the spreading rate and the potential temperature. Interestingly, the average degree of melting in each bin of spreading rate is positively correlated with spreading rate (Fig. 11a). This positive correlation between F and spreading rate has been attributed to deeper final melting depth at slower spreading ridge as a result of strong conductive cooling compared to adiabatic upwelling (Brown and White, 1994; Niu and Hékinian, 1997). Results from the present study suggest that 7% more melting of CIR compared to SWIR (Fig. 11a) at faster spreading ridges could also be partly due to deeper initial melting depth as a result of the 30 °C higher potential temperature.

A reduction of potential temperature from 1310 °C to 1280 °C can explain the observed difference in ε between SWIR and CIR (Figs. 9 and 10). Such variations in potential temperature agree with the ranges of potential temperature inferred from independent studies (Niu and O'Hara, 2008;

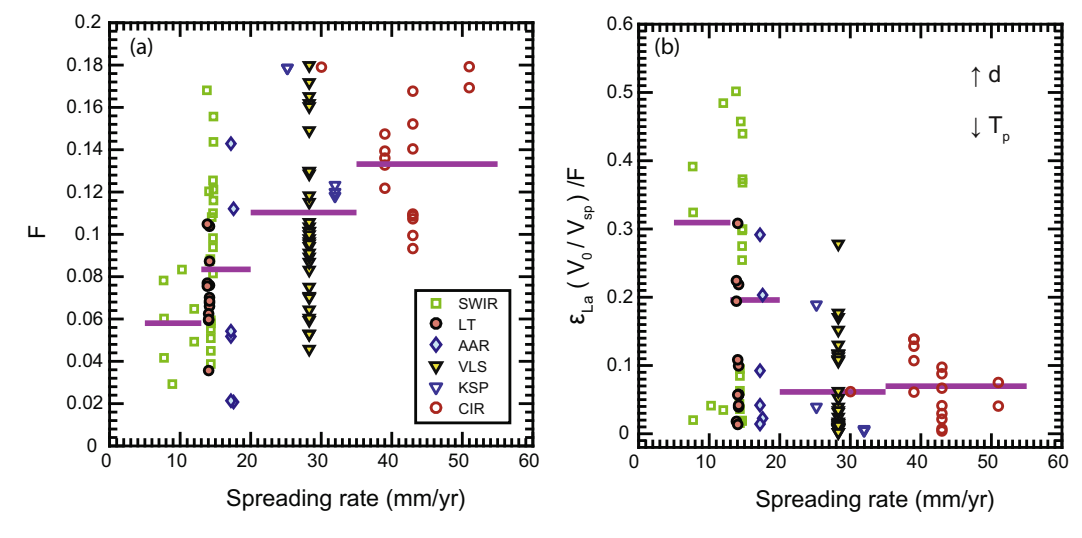


Fig. 11. Plots of inverted degree of melting F (panel a) and normalized disequilibrium parameters ε_{La} (V_0/V_{sp})/F (panel b) as a function of spreading rate. ε_{La} increases with initial grain size (d) and decreases with potential temperature (T_p , marked by arrows in b). The magenta bar represents the average over the interval of spreading rate.

Dalton et al., 2014). Many abyssal peridotite samples are from fracture zones. In Marie Celeste Fracture Zone in CIR, threefold difference of ε exists within 10 km $\varepsilon_{MP} = 0.006^{+0.006}_{-0.004},$ (ANTP89-5: and ANTP87-9: $\varepsilon_{MP} = 0.021^{+0.006}_{-0.005}$). Along the Vema Lithospheric Section at Mid-Atlantic Ridge, the most probable ε appears to vary randomly between 0.0002 and 0.03 (Fig. 12), although the uncertainty does not exclude a constant ε . Such local variation of ε could, in part, be attributed to temperature perturbation associated with transform fault (Morgan and Forsyth, 1988; Roland et al., 2010). If the most probable ε indeed increases 10-fold along this 250 km long fracture zone, this would require a temperature increase of ~ 60 °C. The temperature induced variation of ε is limited by the smoothing effect of thermal diffusion. If the observed variation in ε is due to potential temperature alone, the temperature profile of one sample during melting may be 30 °C higher than the temperature profile of another sample 10 km away. In a thermal model of transform fault (Morgan and Forsyth, 1988; Roland et al., 2010), sharp horizontal temperature gradient is difficult to extend to the depth of initial melting. Therefore temperature can only account for smooth inter-ridge and along-fault variations

The disequilibrium parameter ε_{La} is very sensitive to grain size (Eq. (16)). For the abrupt along-fault variation in ε (Fig. 12), variation or heterogeneity in grain size is a simple explanation. Unfortunately, clinopyroxene which is the dominant host for REE in spinel peridotites is almost exhausted in residual abyssal peridotites (Warren, 2016; and references therein). If the grain size is extrapolated back to the source, the uncertainty is expected to increase further. Here, we provide an estimate of initial grain size of cpx by attributing the local variation of ε at a given F solely to grain size variation after correction for upwelling rate. The factor that regresses inverted data to each predicted melting trend shown in Fig. 10 is proportional to the grain size squared according to Eq. (16). Thus, the grain size of the source is derived for each sample at a presumed potential temperature,

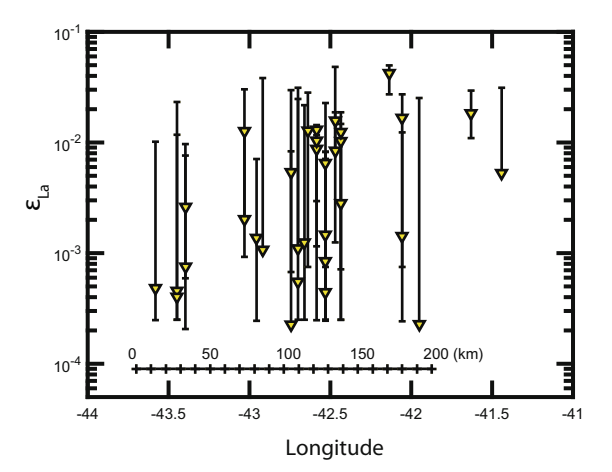


Fig. 12. Variations of ε_{La} in clinopyroxene along the Vema Lithospheric Section at Mid-Atlantic Ridge (trace element data from Brunelli et al., 2006).

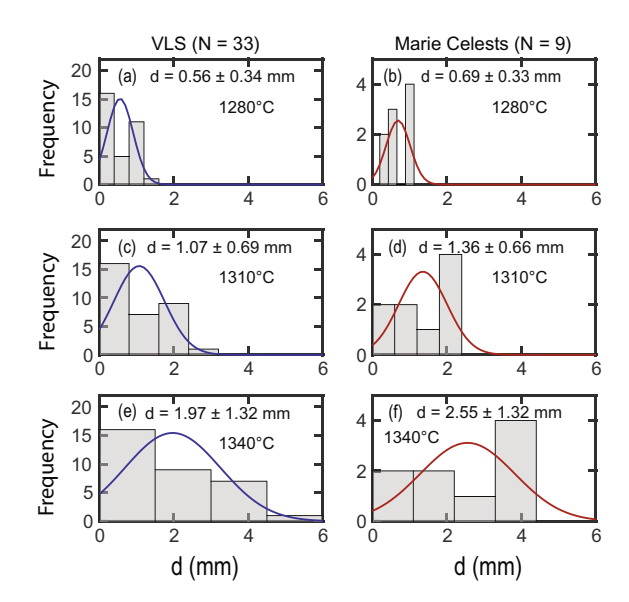


Fig. 13. The grain size distribution of samples from VLS (a, c, e) and Marie Celeste transform fault at CIR (b, d, f) assuming potential temperature of 1280 °C, 1310 °C, or 1340 °C. The average grain size $(\pm\sigma)$ for each case obtained by bootstrap resampling is provided in each panel.

$$d = \sqrt{\frac{\varepsilon_{La} \cdot V_0 / V_{sp}}{\varepsilon_{Tp}^0}} \cdot d_0, \tag{17}$$

where ε_{Tp}^0 is the average ε_{La} calculated along a melting path with potential temperature T_p and reference grain size $(d_0 = 1.5 \text{ mm})$ and reference upwelling rate $(V_0 = 15 \text{ mm/yr})$.

Only samples from the VLS at MAR (Brunelli et al., 2006) and the Marie Celeste TF at CIR (Hellebrand et al., 2002) are used to estimate the average grain size because there is a relatively large dataset within a single transform fault (26 in VLS and 9 in Marie Celeste TF) where we assume the potential temperature is constant. Fig. 13 demonstrates that larger grain size is required to compensate faster diffusion at higher potential temperature. Given three choices of potential temperature, the average grain size ranges from 0.56 mm to 2.55 mm at these two locations. The grain size distribution at these two locations cannot be discriminated statistically given the same potential temperature. In other words, there could be no difference in grain size and potential temperature between these two locations although the spreading rates between the two are somewhat different (Marie Celeste TF, 41 mm/yr; VLS, 28 mm/yr). The average grain size corresponding to each potential temperature is distinct. The potential temperature or the average grain size could be estimated given the knowledge of the other.

5.3. Other processes or factors

A number of factors or processes not considered in the preceding discussion can also affect trace element abundances in residual cpx: (1) source heterogeneity, (2) shallow level refertilization, and (3) subsolidus reequilibration. In

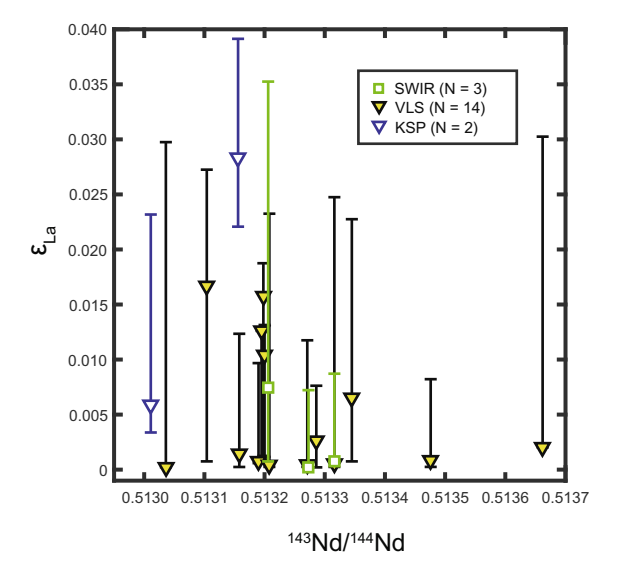


Fig. 14. Diagram showing the lack of correlation between ε_{La} in clinopyroxene and 143 Nd/ 144 Nd in clinopyroxene for 19 samples from the Mid-Atlantic ridge (VLS and KSP) and the Southwest Indian Ridge (SWIR).

Liang and Liu (2016), we assessed the effects of (1) and (2) using available Nd isotope data from VLS (12 samples). Fig. 14 includes 7 additional samples from SWIR, Kane Fracture Zone, and Saint Paul Fracture Zone. There is no obvious correlation between ε and 143 Nd/ 144 Nd, suggesting that mantle source heterogeneity in REE is not an important factor controlling the variation of ε . It is possible that source heterogeneities in major element composition (hence mineral proportion) and cpx grain size also contribute to the observed variations in ε . The former can affect the absolute value of F inverted from the REE data, while the latter has a strong effect on the interpretation of inverted ε (cf. Eq. (16)). There are considerable uncertainties in both. As a first application of MCMC inversion of REE data in residual cpx, our assumption of a DMM initial composition is a reasonable starting point. The size of cpx grains in peridotite is not uniform. During partial melting, smaller cpx grains are likely consumed first. Our inverted ε is likely weighed towards larger cpx grains that control the time scale of diffusive reequilibration between cpx and residual melt. The roles of mantle source heterogeneity and cpx grain size distribution are subjects of future investigations.

Shallow level refertilization by small degree melt produced in the lower part of the melting column has been suggested by Hellebrand et al. (2002) and Brunelli et al. (2006) to account for elevated LREE patterns in residual cpx in some abyssal peridotites from CIR and VLS. We note that refertilization can account for the 34 cpx samples excluded in this study (for examples see Hellebrand et al., 2002; Brunelli et al., 2006; Liang and Liu, 2016).

Elevated HREE patterns in residual cpx in abyssal peridotites have often been attributed to garnet field melting. According to Sun and Liang (2014), HREE in cpx could be elevated by a factor of 2 during subsolidus exchange with orthopyroxene in spinel harzburgite at low temperatures. A correction of HREE to lower values could increase the esti-

mate of F because HREE are more depleted than they appear. The estimate of ε could also increase because there will be more LREE enrichment relative to HREE (see Fig. 5 in Liang and Liu, 2016).

6. SUMMARY AND OUTLOOK

The present study is motivated primarily by the positive correlation between F and ε derived from nonlinear least squares inversion of REE and Y abundances in cpx in abyssal peridotites from CIR using the disequilibrium perfect fractional melting model. To test the robustness of this correlation for melting beneath mid-ocean ridge spreading centers, we used a more general melting model to better assess uncertainties of inverted melting parameters. Most physically more realistic melting models for trace elements do not have explicit analytical solutions, which poses a considerable challenge to inversion of melting parameters through nonlinear least squares analysis of REE data in residual cpx. This led us naturally to the MCMC method. Here we demonstrated the method of MCMC simulations and its advantages in studying geochemical inverse problems through two case studies of disequilibrium mantle melting. We introduced MCMC method to interpret geochemical observations as consequences of the model with unknown physical parameters. We showed that melting parameters inverted through MCMC simulations are consistent with those obtained from direct nonlinear least squares inversions. However, the nonlinear least squares method cannot describe the asymmetric posterior distribution. The uncertainty derived from nonlinear least squares method could be underestimated compared to the MCMC method.

Reading melting parameters from REE data in cpx in abyssal peridotites through MCMC simulations of disequilibrium dynamic melting has led new insights into the melting processes beneath mid-ocean ridge spreading centers. We found that the disequilibrium dynamic melting model (Eqs. (9)–(11)) can explain REE patterns in cpx in 75% residual abyssal peridotite samples considered in this study (101 out of 135). The positive correlation between F and ε_{La} has been confirmed by the disequilibrium dynamic melting model and additional data from several ultra-slow to intermediate spreading centers around the world. We suggest that the positive correlation between F and ε_{La} is a natural consequence of decompressional melting beneath midocean ridge spreading centers (i.e., a continuous competition between melting and diffusive exchange between the minerals and the melt). More isotope and petrological data are needed to assess the role of mantle source heterogeneity on the variations of $\varepsilon_{I,a}$ at a given F. The variation in $\varepsilon_{I,a}$ at a given F is probably not caused by variations in upwelling velocity or spreading rate alone. The combination of potential temperature and grain size distribution of cpx can explain the ε_{La} -F correlations, although additional factors and processes such as mantle source heterogeneity, shallow level refertilization, and subsolidus reequilibration may also contribute to the observed REE patterns in the peridotites.

For the purpose of demonstration, we considered two simple disequilibrium fractional melting models by assuming constant mineral-melt REE partition coefficients and diffusion coefficients, by treating non-modal melting as a simple melting reaction with constant coefficients, and by simplifying the physics of melt extraction with a constant porosity or melt-to-solid mass flux ratio (i.e., the steadystate dynamic melting model). These assumptions and simplifications, which have been widely used in geochemical studies of mantle melting, can be relaxed or eliminated within the framework of MCMC which does not require explicit analytical solutions for the conservation equations. This unique feature of MCMC allows us to use selfconsistent melting models to better constrain melting parameters from trace element abundances in residual minerals and basalts in future studies. For example, in a more realistic scenario of adiabatic mantle melting, one can use a thermodynamic model to calculate residual mineral proportions and major element compositions along a melting path. Results from the thermodynamic modeling can be used to calculate temperature-, pressureand mineral composition-dependent mineral-melt REE partition coefficients and diffusion coefficients based on parameterized lattice strain models for REE partitioning and Arrhenius relations for REE diffusion in pyroxenes. Furthermore, for the one-dimensional steady-state problem considered in this study, it is also straightforward to include the physics of melt migration as part of the MCMC simulations. The melt fraction, melt and solid velocities, and melting rate are related to each other through mass, momentum and energy conservation equations (e.g., McKenzie, 1984; Ribe, 1985; Hewitt and Fowler, 2008). One of the advantages of MCMC methods is that we do not have to know the exact values of porosity and velocity a priori. The uncertainties in these physical parameters can be circumvented by solving forward models with a range of values. The data automatically converge those parameters to the most probable values. With ever increasing computing power and geochemical and geophysical data, it is possible to study a wide range of physically and chemically realistic melting problems through MCMC simulations.

ACKNOWLEDGMENTS

We would like to thank Don Forsyth for advice on MCMC method, Reid Cooper and Greg Hirth for discussion regarding clinopyroxene grain size in mantle rocks, Jessica Warren for sharing of her unpublished SWIR data, and Nick Dygert for a careful reading of an earlier version of this paper. This paper benefited from thoughtful review comments by Paul Asimow, Haibo Zou, an anonymous reviewer, and the associate editor Dmitri Ionov. This work was supported by US National Science Foundation grants OCE-115567 and EAR-1624516 and by NASA grant SSERVI NNA14AB01A.

APPENDIX A. PROCEDURE FOR FINDING σ_- AND Σ_+ FOR PARAMETER F FROM A SET OF ACCEPTED MODELS

To determine σ_{-} and σ_{+} for parameter F from a set of accepted models, we follow the steps outlined below. First, we make the histogram of F with 100 bins. The center of each bin consists of $(F_{b1}, F_{b2}, ..., F_{b100})$. Second, we approx-

imate the histogram of F with a smooth marginal probability density of F, $p_F(F)$. Third, we sort $(F_{b1}, F_{b2}, ..., F_{b100})$ in ascending order of $p_F(F)$ and obtain a set $(F_{bp1}, F_{bp2}, ..., F_{bp100})$. Fourth, we find the smallest index i such that,

$$\sum_{i=i}^{100} pF(F_{bpj}) \leqslant 68\% \cdot \sum_{i=1}^{100} p_F(F_{bpj}). \tag{A1}$$

The minimum and maximum among $(F_{bpi}, F_{bp2}, ..., F_{bp100})$ are F_{lower} and F_{upper} respectively. Finally, we obtain σ_{-} and σ_{+} for parameter F as:

$$\sigma_{-} = F_{MP} - F_{lower} \text{ or } 0 \text{ if } F_{MP} < F_{lower}, \tag{A2}$$

$$\sigma_{+} = F_{upper} - F_{MP} \text{ or } 0 \text{ if } F_{MP} > F_{upper}, \tag{A3}$$

where F_{MP} is the F of the most probable model $\mathbf{m_{MP}}$ among $(\mathbf{m_0}, \mathbf{m_1}, ..., \mathbf{m_n})$.

APPENDIX B. DERIVATION OF THE DISEQUILIBRIUM DYNAMIC MELTING MODEL

We consider trace element fractionation during disequilibrium melting and melt migration in a one-dimensional steady-state upwelling column in which part of the melt generated is extracted to nearby channels or conduits. At steady state, mass conservation equations for a non-radioactive trace element in the interstitial melt, residual solid, and a given mineral in the upwelling matrix are (Liang and Liu, 2016),

$$\rho_f \phi_f V_f \frac{dC_f}{dz} = \Gamma(C_s^p - C_f) + \rho_s (1 - \phi_f) \sum_{j=1}^N w_j R_j (C_s^j - k_j C_f),$$
(B1)

$$\rho_{s}(1 - \phi_{f})V_{s}\frac{dC_{s}}{dz} = \Gamma(C_{s} - C_{s}^{p})$$
$$-\rho_{s}(1 - \phi_{f})\sum_{j=1}^{N}w_{j}R_{j}(C_{s}^{j} - k_{j}C_{f}), \tag{B2}$$

$$\rho_{s}(1-\phi_{f})V_{s}\frac{dC_{s}^{j}}{dz} = -\rho_{s}(1-\phi_{f})R_{j}(C_{s}^{j}-k_{j}C_{f}), \tag{B3}$$

$$C_s = \sum_{i=1}^N x_j C_s^j, \tag{B4}$$

$$C_s^p = \sum_{j=1}^N p_j C_s^j, \tag{B5}$$

$$k = \sum_{j=1}^{N} w_j k_j, \tag{B6}$$

where w_j is the weight fraction of mineral j in residual solid; R_j is the exchange rate constant for the trace element of interest between mineral j and the melt; k_j is the mineral j and melt partition coefficient for the trace element. Definitions of other symbols are listed in Table 1. The first terms on the right-hand side (RHS) of Eqs. (B1), (B2) account for non-modal melting of the solid (the melting term in Eq. (B3) is cancelled out by mass conservation constraint). The second terms on the RHS of Eqs. (B1), (B2) are due to finite rates of mineral-melt mass transfer in the partially molten system. For simplicity, we neglect diffusion and dis-

persion in the melt and use linear kinetics to approximate crystal-melt finite exchange that arises from diffusion in minerals and/or dissolution-reprecipitation (Navon and Stolper, 1987; Richter and DePaolo, 1987; Bodinier et al., 1990; Liang, 2003).

The degree of melting experienced by the solid matrix is given by the material derivative (Liang and Peng, 2010),

$$V_s \frac{dF}{dz} = \frac{(1-F)\Gamma}{\rho_s (1-\phi_f)} \tag{B7}$$

where the factor (1 - F) accounts for the fraction of solid remaining. For the one-dimensional problem considered here, we can rewrite the mass conservation equations in terms of the degree of melting via Eq. (B7) using the chain rule, viz.,

$$\frac{dC}{dz} = \frac{dC}{dF}\frac{dF}{dz} = \frac{(1-F)\Gamma}{\rho_s(1-\phi_f)V_s}\frac{dC}{dF}$$
 (B8)

Substituting Eq. (B8) into Eqs. (B1)–(B3), we have a set of conservation equations relating concentrations to the degree of melting experienced by the solid matrix.

$$\begin{split} &\frac{\rho_{f}\phi_{f}V_{f}}{\rho_{s}(1-\phi_{f})V_{s}}(1-F)\Gamma\frac{dC_{f}}{dF} \\ &= \Gamma(C_{s}^{p}-C_{f}) + \rho_{s}(1-\phi_{f})\sum_{i=1}^{N}w_{j}R_{j}(C_{s}^{j}-k_{j}C_{f}), \end{split} \tag{B9}$$

$$(1-F)\Gamma \frac{dC_s}{dF} = \Gamma(C_s - C_s^p) - \rho_s(1-\phi_f) \sum_{j=1}^{N} w_j R_j(C_s^j - k_j C_f),$$

(B10)

$$(1 - F)\Gamma \frac{dC_s^j}{dF} = -\rho_s (1 - \phi_f) R_j (C_s^j - k_j C_f),$$
 (B11)

For constant melting rate and melt-to-solid mass flux ratio (i.e., in a case of dynamic melting), Eqs. (B9)–(B11) can be further simplified by dividing each equation by the product $\rho_s(1 - \phi_f)R_1$, viz.,

$$\alpha \varepsilon_1 (1 - F) \frac{dC_f}{dF} = \varepsilon_1 (C_s^p - C_f) + \sum_{j=1}^N w_j \frac{R_j}{R_1} (C_s^j - k_j C_f),$$
(B12)

$$\varepsilon_1(1-F)\frac{dC_s}{dF} = \varepsilon_1(C_s - C_s^p) - \sum_{j=1}^N w_j \frac{R_j}{R_1} (C_s^j - k_j C_f),$$
(B13)

$$\varepsilon_1 (1 - F) \frac{dC_s^j}{dF} = -\frac{R_j}{R_1} (C_s^j - k_j C_f),$$
 (B14)

where α is the melt-to-solid mass flux ratio (Eq. (12)); ε_1 is the disequilibrium parameter defined with respect to the exchange rate constant for the element of interest in mineral 1.

$$\varepsilon_1 = \frac{\Gamma}{\rho_s (1 - \phi_f) R_1}. ag{B15}$$

When $R_1 = R_2 = ... = R_N = R$, Eqs. (B12)-(B14) reduce to Eqs. (9)-(11) which are the working model in this study.

APPENDIX C. SUPPLEMENTARY DATA

Supplementary data associated with this article can be found, in the online version, at http://dx.doi.org/10.1016/j.gca.2016.12.040.

REFERENCES

Albarède F. (1995) Introduction to Geochemical Modeling. Cambridge University Press.

Allegre C. and Minster J. (1978) Quantitative models of trace element behavior in magmatic processes. *Earth Planet. Sci. Lett.* 38, 1–25.

Anders E. and Grevesse N. (1989) Abundances of the elements: meteoritic and solar. *Geochim. Cosmochim. Acta* **53**, 197–214.

Argus D. F. and Gordon R. G. (1991) No-net-rotation model of current plate velocities incorporating plate motion model NUVEL-1. Geophys. Res. Lett. 18, 2039–2042.

Asimow P. D., Hirschmann M. M. and Stolper E. M. (1997) An analysis of variations in isentropic melt productivity. *Philos. Trans. Royal Soc. Lond. A: Mathem. Phys. Eng. Sci.* 355, 255–281.

Asimow P. D., Hirschmann M. M. and Stolper E. M. (2001) Calculation of Peridotite partial melting from thermodynamic models of minerals and melts, IV. Adiabatic decompression and the composition and mean properties of mid-ocean Ridge Basalts. *J. Petrol.* **42**, 963–998.

Backus G. and Gilbert F. (1968) The resolving power of gross earth data. *Geophys. J. Roy. Astron. Soc.* **16**, 169–205.

Baker M. B. and Stolper E. M. (1994) Determining the composition of high-pressure mantle melts using diamond aggregates. Geochim. Cosmochim. Acta 58, 2811–2827.

Bodinier J. L., Vasseur G., Vernieres J., Dupuy C. and Fabries J. (1990) Mechanisms of mantle metasomatism: geochemical evidence from the Lherz orogenic peridotite. *J. Petrol.* **31**, 597–628.

Brown J. W. and White R. S. (1994) Variation with spreading rate of oceanic crustal thickness and geochemistry. *Earth Planet. Sci. Lett.* 121, 435–449.

Brunelli D. and Seyler M. (2010) Asthenospheric percolation of alkaline melts beneath the St. Paul region (Central Atlantic Ocean). Earth Planet. Sci. Lett. 289, 393–405.

Brunelli D., Seyler M., Cipriani A., Ottolini L. and Bonatti E. (2006) Discontinuous melt extraction and weak refertilization of mantle peridotites at the Vema Lithospheric Section (Mid-Atlantic Ridge). J. Petrol. 47, 745–771.

Brunelli D., Paganelli E. and Seyler M. (2014) Percolation of enriched melts during incremental open-system melting in the spinel field: a REE approach to abyssal peridotites from the Southwest Indian Ridge. Geochim. Cosmochim. Acta 127, 190– 203

Dalton C. A., Langmuir C. H. and Gale A. (2014) Geophysical and geochemical evidence for deep temperature variations beneath mid-ocean ridges. *Science* 344, 80–83.

DeMets C., Gordon R. G. and Argus D. F. (2010) Geologically current plate motions. *Geophys. J. Int.* **181**, 1–80.

Feigenson M. D. and Carr M. J. (1993) The Source Of Central-American lavas – inferences from geochemical inverse modeling. Contrib. Miner. Petrol. 113, 226–235.

Feigenson M. D., Hofmann A. W. and Spera F. J. (1983) Case studies on the origin of basalt. 2. The transition from tholeitic ot alkalic volcanism on Kohala volcano, Hawaii. *Contribut. Mineral. Petrol.* 84, 390–405.

Ghiorso M. S., Hirschmann M. M., Reiners P. W. and Kress V. C. (2002) The pMELTS: a revision of MELTS for improved

- calculation of phase relations and major element partitioning related to partial melting of the mantle to 3 GPa. *Geochem. Geophys. Geosyst.* **3**, 1–35.
- Grandis H., Menvielle M. and Roussignol M. (1999) Bayesian inversion with Markov chains—I. The magnetotelluric onedimensional case. *Geophys. J. Int.* 138, 757–768.
- Hastings W. K. (1970) Monte Carlo sampling methods using Markov chains and their applications. *Biometrika* **57**, 97–109.
- Hellebrand E. and Snow J. E. (2003) Deep melting and sodic metasomatism underneath the highly oblique-spreading Lena Trough (Arctic Ocean). Earth Planet. Sci. Lett. 216, 283–299.
- Hellebrand E., Snow J. E., Hoppe P. and Hofmann A. W. (2002) Garnet-field melting and late-stage refertilization in 'residual' abyssal peridotites from the Central Indian Ridge. *J. Petrol.* 43, 2305–2338.
- Hewitt I. J. and Fowler A. C. (2008) Partial melting in an upwelling mantle column. *Proc. R. Soc. A* 464, 2467–2491.
- Hofmann A. W. and Feigenson M. D. (1983) Case studies on the origin of basalt. I. Theory and reassessment of Grenada basalts. *Contrib. Miner. Petrol.* 84, 382–389.
- Iwamori H. (1993a) Dynamic disequilibrium melting model with porous flow and diffusion-controlled chemical equilibration. *Earth Planet. Sci. Lett.* 114, 301–313.
- Iwamori H. (1993b) A model for disequilibrium mantle melting incorporating melt transport by porous and channel flows. *Nature* 366, 734–737.
- Iwamori H. (1994) 238U–230Th-226Ra and 235U–231Pa disequilibria produced by mantle melting with porous and channel flows. Earth Planet. Sci. Lett. 125, 1–16.
- Johnson K. T. M., Dick H. J. B. and Shimizu N. (1990) Melting in the oceanic upper mantle: an ion microprobe study of diopsides in abyssal peridotites. J. Geophys. Res.: Solid Earth 95, 2661– 2678
- Jull M., Kelemen P. B. and Sims K. (2002) Consequences of diffuse and channelled porous melt migration on uranium series disequilibria. Geochim. Cosmochim. Acta 66, 4133–4148.
- Kelemen P. B., Hirth G., Shimizu N., Spiegelman M. and Dick H. J. B. (1997) A review of melt migration processes in the adiabatically upwelling mantle beneath oceanic spreading ridges. *Philos. Trans.: Mathem., Phys. Eng. Sci.* 355, 283–318.
- Kelley K. A., Plank T., Grove T. L., Stolper E. M., Newman S. and Hauri E. (2006) Mantle melting as a function of water content beneath back-arc basins. *J. Geophys. Res.: Solid Earth* 111.
- Korenaga J. and Karato S.-I. (2008) A new analysis of experimental data on olivine rheology. J. Geophys. Res.: Solid Earth 113, B02403.
- Langmuir C. H., Bender J. F., Bence A. E., Hanson G. N. and Taylor S. R. (1977) Petrogenesis of basalts from the FAMOUS area: Mid-Atlantic Ridge. *Earth Planet. Sci. Lett.* 36, 133–156.
- Langmuir C., Bezos A., Escrig S. and Parman S. (2006) Hydrous mantle melting at ridges and back-arc basins. *Geochim. Cosmochim. Acta* 70, A341.
- Lassiter J. C., Byerly B. L., Snow J. E. and Hellebrand E. (2014) Constraints from Os-isotope variations on the origin of Lena Trough abyssal peridotites and implications for the composition and evolution of the depleted upper mantle. *Earth Planet. Sci. Lett.* 403, 178–187.
- Liang Y. (2003) On the thermo-kinetic consequences of slab melting. *Geophys. Res. Lett.* 30, 2270. http://dx.doi.org/ 10.1029/2003GL018969.
- Liang Y. and Liu B. (2016) Simple models for disequilibrium fractional melting and batch melting with application to REE fractionation in abyssal peridotites. *Geochim. Cosmochim. Acta* 173, 181–197.
- Liang Y. and Parmentier E. M. (2010) A two-porosity double lithology model for partial melting, melt transport and melt-

- rock reaction in the mantle: mass conservation equations and trace element transport. *J. Petrol.* **51**, 125–152.
- Liang Y. and Peng Q. (2010) Non-modal melting in an upwelling mantle column: steady-state models with applications to REE depletion in abyssal peridotites and the dynamics of melt migration in the mantle. *Geochim. Cosmochim. Acta* 74, 321– 339.
- Liu J. S. (2008) Monte Carlo Strategies in Scientific Computing. Springer Science & Business Media.
- Lundstrom C. (2000) Models of U-series disequilibria generation in MORB: the effects of two scales of melt porosity. *Phys. Earth Planet. Inter.* **121**, 189–204.
- Mallick S., Dick H. J. B., Sachi-Kocher A. and Salters V. J. M. (2014) Isotope and trace element insights into heterogeneity of subridge mantle. *Geochem. Geophys. Geosyst.* 15, 2438–2453.
- McKenzie D. (1984) The generation and compaction of partially molten rock. *J. Petrol.* **25**, 713–765.
- McKenzie D. (1985) ²³⁰Th-²³⁸U disequilibrium and the melting processes beneath ridge axes. *Earth Planet. Sci. Lett.* **72**, 149–157.
- McKenzie D. and O'Nions R. K. (1991) Partial melt distributions from inversion of rare earth element concentrations. *J. Petrol.* **32**, 1021–1091.
- McKenzie D. and O'Nions R. K. (1995) The source regions of ocean island basalts. *J. Petrol.* **36**, 133–159.
- McKenzie D. and O'Nions R. K. (1998) Melt production beneath oceanic islands. *Phys. Earth Planet. Inter.* **107**, 143–182.
- McKenzie D., Stracke A., Blichert-Toft J., Albarede F., Gronvold K. and O'Nions R. K. (2004) Source enrichment processes responsible for isotopic anomalies in oceanic island basalts. *Geochim. Cosmochim. Acta* **68**, 2699–2724.
- Metropolis N., Rosenbluth A. W., Rosenbluth M. N., Teller A. H. and Teller E. (1953) Equation of state calculations by fast computing machines. *J. Chem. Phys.* **21**, 1087–1092.
- Minster J. F. and Allegre C. J. (1978) Systematic use of traceelements In igneous processes. III. Inverse problem of batch partial melting in volcanic suites. *Contrib. Miner. Petrol.* 68, 37– 52
- Morgan J. P. and Forsyth D. W. (1988) Three-dimensional flow and temperature perturbations due to a transform offset: effects on oceanic crustal and upper mantle structure. *J. Geophys. Res.: Solid Earth* **93**, 2955–2966.
- Navon O. and Stolper E. (1987) Geochemical consequences of melt percolation: the upper mantle as a chromatographic column. *J. Geol.* **95**, 285–307.
- Niu Y. (2004) Bulk-rock major and trace element compositions of abyssal peridotites: implications for mantle melting, melt extraction and post-melting processes beneath mid-ocean ridges. *J. Petrol.* **45**, 2423–2458.
- Niu Y. and Hékinian R. (1997) Spreading-rate dependence of the extent of mantle melting beneath ocean ridges. *Nature* **385**, 326–329.
- Niu Y. and O'Hara M. J. (2008) Global correlations of ocean ridge basalt chemistry with axial depth: a new perspective. *J. Petrol.* **49**, 633–664.
- Ormerod D. S., Rogers N. W. and Hawkesworth C. J. (1991) Melting in the lithospheric mantle – inverse modeling of alkaliolivine basalts from the Big Pine volcanic field, California. Contrib. Miner. Petrol. 108, 305–317.
- Ozawa K. (2001) Mass balance equations for open magmatic systems: trace element behavior and its application to open system melting in the upper mantle. *J. Geophys. Res.: Solid Earth* **106**, 13407–13434.
- Parker R. L. (1977) Understanding inverse theory. *Annu. Rev. Earth Planet. Sci.* **5**, 35.

- Qin Z. (1992) Disequilibrium partial melting model and its implications for trace element fractionations during mantle melting. Earth Planet. Sci. Lett. 112, 75–90.
- Ribe N. M. (1985) The deformation and compaction of partial molten zones. *Geophys. J. Int.* **83**, 487–501.
- Richter F. M. (1986) Simple models for trace element fractionation during melt segregation. *Earth Planet. Sci. Lett.* 77, 333–344.
- Richter F. M. and DePaolo D. J. (1987) Numerical models for diagenesis and the Neogene Sr isotopic evolution of seawater from DSDP Site 590B. Earth Planet. Sci. Lett. 83, 27–38.
- Robert C. and Casella G. (2004) *Monte Carlo Statistical Methods*, second ed. Springer Science & Business Media.
- Roland E., Behn M. D. and Hirth G. (2010) Thermal-mechanical behavior of oceanic transform faults: implications for the spatial distribution of seismicity. *Geochem. Geophys. Geosyst.* 11. http://dx.doi.org/10.1029/2010GC003034.
- Salters V. J. M. and Dick H. J. B. (2002) Mineralogy of the midocean-ridge basalt source from neodymium isotopic composition of abyssal peridotites. *Nature* 418, 68–72.
- Sambridge M. and Mosegaard K. (2002) Monte Carlo methods in geophysical inverse problems. *Rev. Geophys.* **40**, 1009.
- Seyler M., Brunelli D., Toplis M. J. and Mével C. (2011) Multiscale chemical heterogeneities beneath the eastern Southwest Indian Ridge (52 °E – 68 °E): Trace element compositions of alongaxis dredged peridotites. *Geochem. Geophys. Geosyst.* 12. http:// dx.doi.org/10.1029/2011GC003585.
- Shaw D. M. (2000) Continuous (dynamic) melting theory revisited. *Canadian Mineral.* **38**, 1041–1063.
- Shaw D. M. (2006) Trace Elements in Magmas: A Theoretical Treatment. Cambridge University Press.
- Shimizu N. (1998) The geochemistry of olivine-hosted melt inclusions in a FAMOUS basalt ALV519-4-1. *Phys. Earth Planet. Inter.* 107, 183–201.
- Shu C.-W. and Osher S. (1988) Efficient implementation of essentially non-oscillatory shock-capturing schemes. *J. Comput. Phys.* 77, 439–471.
- Smith P. M. and Asimow P. D. (2005) Adiabat_1ph: A new public front-end to the MELTS, pMELTS, and pHMELTS models. Geochem. Geophys. Geosyst. 6. http://dx.doi.org/10.1029/ 2004GC000816.
- Spiegelman M. and Kelemen P. B. (2003) Extreme chemical variability as a consequence of channelized melt transport.

- Geochem. Geophys. Geosyst. **4**. http://dx.doi.org/10.1029/2002GC000336.
- Sun C. and Liang Y. (2014) An assessment of subsolidus reequilibration on REE distribution among mantle minerals olivine, orthopyroxene, clinopyroxene, and garnet in peridotites. *Chem. Geol.* 372, 80–91.
- Tainton K. M. and McKenzie D. (1994) The generation of kimberlites, lamproites, and their source rocks. J. Petrol. 35, 787–817.
- Tarantola A. (2005) Inverse problem theory and methods for model parameter estimation. Society for Industrial and Applied Mathematics, Philadelphia, PA.
- Van Orman J. A., Grove T. L. and Shimizu N. (2002) Diffusive fractionation of trace elements during production and transport of melt in Earth's upper mantle. *Earth Planet. Sci. Lett.* 198, 93–112.
- Warren J. M. (2007) Geochemical and rheological constraints on the dynamics of the oceanic upper mantle (Ph.D. thesis). Massachusetts Institute of Technology/Woods Hole Oceanographic Institute.
- Warren J. M. (2016) Global variations in abyssal peridotite compositions. *Lithos* 248–251, 193–219.
- Watson S. (1993) Rare earth element inversions and percolation models for Hawaii. J. Petrol. 34, 763–783.
- Watson S. and McKenzie D. (1991) Melt generation by plumes a study of Hawaiian volcanism. *J. Petrol.* **32**, 501–537.
- White R. S., McKenzie D. and O'Nions R. K. (1992) Oceanic crustal thickness from seismic measurements and rare earth element inversions. *J. Geophys. Res.: Solid Earth* **97**, 19683–19715
- Workman R. K. and Hart S. R. (2005) Major and trace element composition of the depleted MORB mantle (DMM). Earth Planet. Sci. Lett. 231, 53–72.
- Zou H. (1998) Trace element fractionation during modal and nonmodal dynamic melting and open-system melting: a mathematical treatment. Geochim. Cosmochim. Acta 62, 1937–1945.
- Zou H. (2007) Quantitative Geochemistry. Imperial College Press, London, UK.

Associate editor: Dmitri A. Ionov